2014

Photophysical properties and interactions in Single Wall Nanotube - DNA - Rare Earth systems

Tetyana Ignatova
Lehigh University

Photophysical properties and interactions in Single Wall Nanotube - DNA - Rare Earth systems

by

Tetyana Ignatova

A Dissertation
Presented to the Graduate Committee
of Lehigh University
in Candidacy for the Degree of
Doctor of Philosophy
in
Physics

Lehigh University
January 2014

Approved and recommended for acceptance as a dissertation in partial fulfillment of the requirements for the degree of Doctor of Philosophy.

Tetyana Ignatova
Photophysical properties and interactions in Single Wall Nanotube - DNA - Rare Earth systems

---

Defense Date

Slava V. Rotkin, Dissertation Director, Chair

Accepted Date

Committee Members

Volkmar R. Dierolf

Ivan Biaggio

Michael J. Stavola

Anand Jagota

Acknowledgement

I wish to express my heartfelt gratitude to my advisor Prof. Slava V. Rotkin for his guidance and support during my Ph.D. study, not only professionally, but personally as well. Many thanks to all members of my dissertation committee for the useful suggestions they provided and for being very cooperative. I would like to thank the entire physics faculty and staff for making my stay at Lehigh successful, to Lois and Pam for their kind support. I thank all the members of the Rotkin's group, they contributed significantly to my growth and development as a researcher with the exchanging of ideas: Massooma Pirbhai, Mike Blades, Andrei Nemilentsau, Ben Sofka, Dan You, Tom Flores, Ben Tayo. I thank my family for their love and encouragement.

Contents

List of Tables

List of Figures

Abstract

The studies of Single Wall Nanotube (SWNT) complexes may be important for development of bio-compatible materials as well as future generations of electronic and optical devices. For bio-marker applications the complexes of SWNTs with Rare Earth ions (REIs) are of large interest. Significant acceleration of the REI photoluminescence (PL) decay rate was observed in water solutions of complexes of rare earth ions, Tb and Eu, with SWNTs. We propose that the time-resolved PL spectroscopy data are explained by a fluorescence resonance energy transfer (FRET) between the REIs and SWNTs. Similar FRET was also studied between two REIs (in the absence of nanotubes). In these experiments FRET was directly confirmed by detecting the induced PL of the energy acceptor, Eu ion, under the PL excitation of the donor ion, Tb. FRET efficiency reached 7% in the most saturated solution, where the distance between the unlike REIs is the shortest. Using this as a calibration experiment, a comparable FRET was measured in the mixed solution of REIs with SWNTs wrapped with DNA. From the FRET efficiency of 10% and 7% for Tb and Eu, respectively, the characteristic distance between the REI and SWNT/DNA was obtained as 15.9 Å independent of concentration of species. Such a short distance suggests that the complexes are formed. Coulomb attraction between the REI and the ionized phosphate groups of the DNA is proposed as the mechanism of the complex formation.

SWNT samples often made with the help of surfactants other then DNA. For example, DOC was successfully used to disperse SWNTs in water solutions. Here the interactions of REIs with DOC were studied. Formation of stable complexes of REIs and DOC and their evolution in a crowded environment of silica hydrogels are described. By comparing the behaviour of REI complexes in bulk solution and small compartments inside the hydrogel the nature of the 5x-longer lifetime of REIs was understood. The effect is due to binding of REI to surfactant molecules followed by formation of a closed shell micelle, completely or partially screening REI from the water molecules. Formation of DOC micelles is accompanied by diffusion of REI between/through the micelles. The process is shown to be slowed down in the

crowded environment of a hydrogel.

Multi-wavelength excitation was applied to study the interaction of SWNT with the DNA, excited by UV light. An additional non-radiative recombination channel, created by the photo-ionized DNA was found. In two-color excitation scheme, by combining a standard visible excitation with an additional UV pump, $G_{vis} + G_{UV}$, which can be tuned to the resonant excitation of ssDNA, unexpected quenching of SWNT PL was observed for all SWNT species presented in solution.

Chapter 1

Introduction

SWNT have been studied intensely since their discovery two decades ago [3, 4]. They are made of an infinitesimally thin graphite layer (just one atomic layer thick) rolled up into a hollow cylinder and their optical and electronic properties depend on particular chiral structure. Fig.1.1a shows the graphene honeycomb-shape atomic lattice. Here, the unit cell can be described by the two unit vectors $\mathbf{a_1}$ and $\mathbf{a_2}$. In case of SWNT the graphene lattice vector $\mathbf{c} = n\mathbf{a_1} + m\mathbf{a_2}$ becomes the circumference of the tube. The circumference vector $\mathbf{c}$ is called the chiral vector. It is completely determined by the pair of integers (n, m), which uniquely define a particular tube. The diameter of the tube is given by the length of the chiral vector:

$$d = \frac{|c|}{\pi} = \frac{a_0}{\pi}\sqrt{n^2 + nm + m^2},$$

where $a_0 = 2.461$Å is the length of a carbon–carbon chemical bond. Depending of the indices (n, m), SWNTs can be metals (when $(n - m) \mod 3 = 0$) and semiconductors ($(n - m) \mod 3 = \pm 1$). Because of its one-dimensionality (1D), a SWNT imparts strong quantum confinement and weak dielectric screening. Therefore the Coulomb interaction strength is large compared with conventional solids. Optical transitions in nanotubes are dominated by correlated electron-hole bound states known as *excitons* [5–7]. The properties of excitons define various optical phenomena observed in SWNT [8–12]: optical absorption, photoluminescence (PL), Raman scattering.

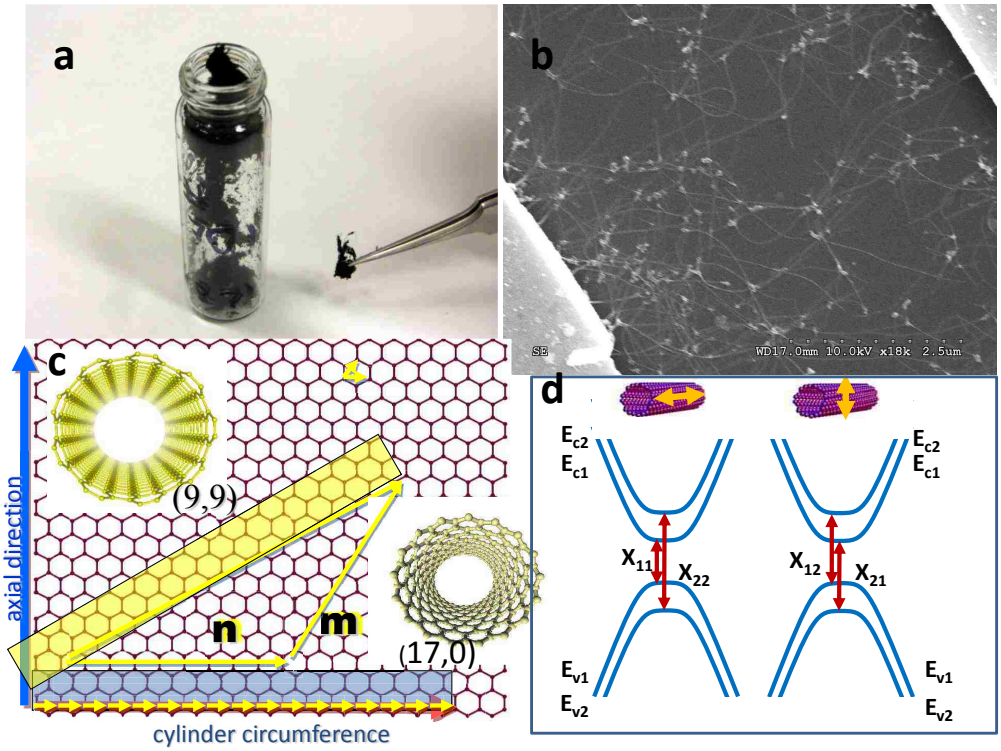

Figure 1.1: (a) Dry CoMoCat SWNT; (b) SEM picture of SWNT; (c) Graphene honeycomb lattice with the lattice vectors a_1 and a_2. The unit cells of two SWNTs with their chiral vectors $c = 9a_1 + 9a_2$ (yellow rectangle) and $c = 17a_1 + 0a_2$ (blue rectangle) are plotted. (d) Schematic of the optical selection rules and band structure of SWNT.

For future industrial application of SWNTs as nanoscale light emitters in telecommunications, bioimaging, etc., it is important to understand the photophysical properties of nanotubes as well as the complexes based on nanotubes.

1.1 Excitons in SWNTs

The interaction of solids with the light can be described by the polarization vector field, **P**, which is induced by the externally applied electric field, **E**. The dielectric response of a solid-state system is given by the complex dielectric function $\epsilon(\omega)$,

which relates the displacement vector, $\mathbf{D}$, to the incoming electric field:

$$D(\omega) = \epsilon(\omega)E(\omega) = [\epsilon_1(\omega) + i\epsilon_2(\omega)]E(\omega),$$

where ϵ_1 and ϵ_2 are the real and imaginary parts of the dielectric function. The latter can be calculated from the experimentally measured absorption coefficient via:

$$\alpha = \frac{2\kappa\omega}{c} = \frac{\epsilon_2\omega}{nc},$$

where c is the speed of light, and n and κ are the refractive index and extinction coefficient respectively. The latter two are related to the components of the dielectric function via the complex refraction index which is by definition:

$$\chi = n + i\kappa = \sqrt{\epsilon_1 + i\epsilon_2}$$

or, taking the square of it:

$$\epsilon_1 = n^2 - \kappa^2 \quad \text{and} \quad \epsilon_2 = 2n\kappa.$$

If the refractive index is constant, $\alpha(\omega)$ is completely defined by the imaginary part of the dielectric function $\epsilon_2(\omega)$.

Within the dipole approximation ϵ_2 depends on dispersion relation of charge carriers in the valence $E_v(\mathbf{k})$ and conduction $E_c(\mathbf{k})$ bands, as well as on the dipole matrix element $|M_{cv}(\mathbf{k})|$ of optical transition between them:

$$\epsilon_2(\omega) = \left(\frac{2\pi e}{m\omega}\right)^2 \sum_{\mathbf{k}} |M_{cv}(\mathbf{k})|^2 \delta(E_c(\mathbf{k}) - E_v(\mathbf{k}) - \hbar\omega).$$

If we can neglect the $\mathbf{k}$ dependence of the matrix element, the expression for the imaginary part of the dielectric function simplifies to:

$$\epsilon_2(\omega) = \left(\frac{2\pi e}{m\omega}\right)^2 |M_{cv}|^2 n_j(E) \tag{1.1}$$

where $n_j(E)$ is the joint density of states (JDOS) of both the conduction and valence bands.

A schematic representation of the SWNT band structure in momentum space and an optical transition are sketched on Fig.1.1 The optical selection rules for transitions are defined, in principle, by the symmetry of a particular nanotube. However the relative polarization of the electric field vector to the nanotube axis is fixed. In all SWNTs the electron-hole symmetry results in the same angular momentum quantum number for the conduction and valence subbands numbered correspondingly up and down from the midgap energy level. The momentum conservation law ($\triangle \mathbf{k} \approx 0$) for the optical excitation requires both the axial momentum of the excitation and its angular momentum to be zero. Thus the excitation produced by a photon with the polarization parallel to the SWNT axis and having the dipole moment parallel to the axis, must have full cylindrical symmetry of the wave function. This requires the electron and hole to have the same angular momentum around the nanotube circumference, adding to zero. These transitions are shown as X_{ii}, with $i = 1, 2, \ldots$ in Fig.1.1.

As mentioned previously the optical transitions in SWNT are driven by excitons, and those selection rules also apply to excitons. As a result, the E_{ii} exciton has zero angular momentum. These excitons are responsible for major optical features of SWNT absorption and emission. In addition, there are the excitons with circular (perpendicular) polarization of the dipole moment, that can be excited by photons cross-polarized to the SWNT axis. This perpendicularly polarized absorption is suppressed by the depolarization effect.

Another feature of SWNT excitons is its large binding energy. The Coulomb interaction in general has larger influence on the optical spectra of semiconductors at low dimensionality. The binding energy for the bound electron-hole pair in pure 1D system diverges [13]. This (non-physical) divergence is suppressed in SWNTs by the finite radius of the tube, which presents a cut off size. Not surprisingly, the size of the exciton will be also close to this length. Moreover, the oscillator strength and coupling of exciton states to other modes is also strongly affected by dimensionality.

The free carrier electron-hole (e-h) continuum is modified by Coulomb interaction in the way illustrated schematically in Fig.1.2. Reflecting the one dimensionality of SWNT, the density of states (DOS) exhibits the van Hove singularity at the band

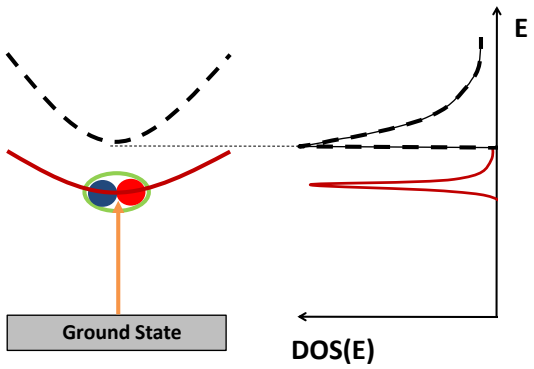

Figure 1.2: Schematic representation of the many-body manifold of the first SWNT subband (left) and corresponding density of states (DOS) (right). The lowest exciton level is shown by red curve, the free electron-hole continuum is shown by black (dashed) curve.

edge. The optical transitions should occur between the Van Hove peaks in the one-electron picture (without Coulomb interaction taken into account). Let us consider the effect of strong electronic many-body interactions. It has been predicted that in 1D semiconductors, optical resonances occur at the wavelength corresponding to exciton energy levels, instead of van Hove singularities corresponding to free e-h continuum. Under light illumination, electrons and holes are generated by resonant absorption of photons. They interact instantaneously by the Coulomb force and form a two-particle bound-state (exciton) stabilized by the binding energy E_b. Thus the absorption peak red-shifts with respect to idealistic picture of non-interacting particles.

In a 1D system, the exciton binding energy is found to be much larger then in 3D systems. Binding energy in SWNT with 1 nm diameter is around 0.5-1.0 eV [14] while in bulk semiconductors at room temperature it is of the order of a few to a few tens of meV. The binding energy reflects the size of the exciton (e-h separation); for a nanotube with 1 nm diameter, the exciton size is $\sim$ 2nm, according to recent

publications [15, 16].

The Coulomb interaction in 1D also increases the oscillator strength of optical transitions. According to the Thomas-Reiche-Kuhn sum rule the total oscillator strength of all transitions from state a to state b is conserved:

$$\sum_b f_{ab} = Z$$

where Z is in a number of electrons participating in the transition. Therefore, increasing of the oscillator strength of excitons will result in decreasing of the oscillating strength of the free e-h continuum. Ando [5] was the first who predicted the formation of strongly bound excitonic states in SWNTs with the oscillator strength moved to these levels from the continuum due to the Coulomb interaction.

The symmetry of the lattice of graphene results in degeneracy in momentum space: two points in the first Brillouin zone, K and K', have the same band structure, up to chirality of the charge carriers. Symmetry adapted combinations of e-h pairs at KK and $K'K'$ are responsible for the formation of bright and dark excitons, combinations $K'K$ and KK' are responsible for K-split indirect excitons. Excitons with non-zero angular momentum may also show a small absorption/emission peak, due to lifting of the selection rules by co-absorption/co-emission of SWNT phonons. In addition to this 4-fold symmetry, the combination of spins of electron and the hole, allows 4 singlet and 4 triplet excitons with different symmetry properties and energies [17, 18]. Among these states the only one exciton state can be optically allowed and is labeled as the 'bright' exciton. All others are optically forbidden states.

1.2 Sample preparation

The understanding of SWNT electronic structure and optical properties was facilitated by progress in sample preparation. Several techniques are used to grow nanotubes [19–21]: laser ablation, catalytic chemical vapor deposition (CVD), arc-discharge, high-pressure carbon monoxide disproportionation (HiPco) CVD. All techniques are mostly producing SWNT material in nanotube bundles.

The absorption spectra of bundles show very broad bands in the visible and NIR range. The PL of NTs in bundles is difficult to observe due to rapid nonradiative decay of excitons in semiconducting nanotubes into metallic ones or semiconducting with the smaller band gap [22, 23]. Development of methods for the separation of bundles received a great attention. O'Connell [24] was the first who developed the method of dispersing SWNT in micelles using sodium dodecyl sulfate (SDS) surfactant in D_2O (or water) and detected the clearly resolved band gap emission from individual semiconducting SWNT. These samples were composed of mutually isolated and well separated tubes, or small nanotubes aggregates which were encapsulated in surfactant micelles.

The typical dispersion process involves sonication and removal of the residual bundles by ultracentrifugation. Then the supernatant includes individually dispersed SWNTs. Various techniques for isolation of individual SWNTs and separation them from bundles have been intensively studied, and various surfactants, including organic salts [25,26] Fig.1.3bc, DNA [27,28] Fig.1.3a, polymers and organic molecules [29–32] have been proposed for efficient dispersion of SWNTs. Further development of sample purity and structural selectivity were obtained by density gradient ultracentrifugation (DGU). It allows to sort nanotube suspension by aggregate size, diameter, chirality and metallicity [33, 34]. Today, one of the remaining problems in the dispersion procedure is nanotube damage during rigorous sonification process and relatively low yields for the highest purity (electronic grade) material.

1.3 Optical absorption cross section

We can estimate the SWNT concentration in the solution, c, from the extinction coefficient $\alpha = \epsilon_c \nu c$, where ϵ_c is the carbon atom molar extinction coefficient and ν is the average number of carbon atoms per tube. The extinction coefficient $\epsilon_c = \sigma_C^{SWNT} N_A$ can be estimated from carbon atom absorption cross section at E_{11} or E_{22} SWNT resonance, σ_C^{SWNT}, which is about 1×10^{-17} cm^2/atom [35, 36].

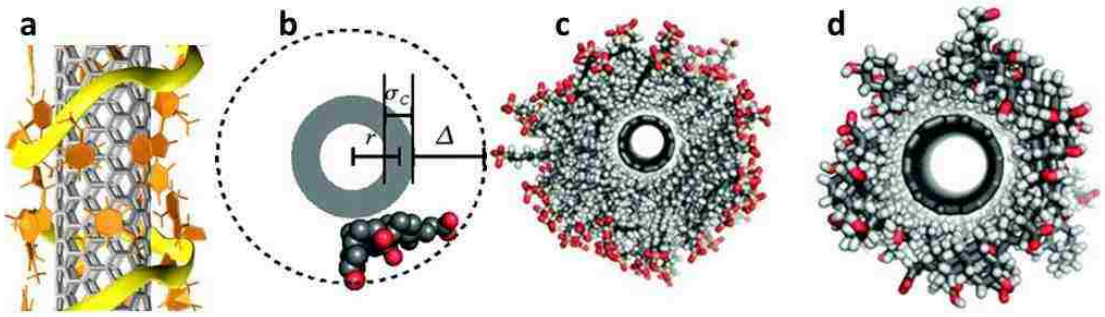

Figure 1.3: (a) DNA wrapped SWNT (Tu *et al*, Nature, 2009); (b) cholate molecule from a SWNT surrounding. Cross-sections of stabilized SWNT-surfactant systems for: (c) SDS and (d) cholate (A. Quintill et. al., 2010)

The resonance absorption cross section (measured exactly at the exciton energy) must be related to the spectral absorption coefficient which now depends on the estimate for the width of the absorption peak. Therefore, the oscillator strength per carbon atom, which is proportional to the integrated absorption coefficient in the vicinity of a single transition of SWNTs, is more fundamental as a photophysical parameter. The oscillator strength per carbon atom, f_0, has been theoretically predicted to be $f_0 = (0.014eV^{-1})E_{ex}$, where E_{ex} denotes the exciton energy (for example for the first subband, $E_{ex} = E_{11}$). Recently, f_0 of the E_{11} bright exciton in (6, 5) SWNT has been experimentally evaluated to be ~ 0.01, which is of the same order of magnitude as in the theoretical prediction for $E_{11} = 1.25$ eV.

The 2D photoluminescence/photoluminescence excitation maps (PL/PLE maps) are commonly used in optical characterization of SWNT samples containing several chirality species. It is more convenient for the structural assignment of E_{ii} subband features than separately taken absorption and emission spectra. In such a graph the SWNT emission intensity is plotted as a function of the excitation and emission photon wavelengths. PL/PLE maps give visual correlation between absorption and emission spectra, which are characteristic for each (n,m) indexes.

Fig.1.4 presents a typical PL/PLE map of CoMoCat SWNT wrapped with DNA and dissolved in D_2O. The small Stokes shift is typical for SWNT solutions. The E_{11}

emission energy is seen in PL at about 4 nm shift with respect to absorption feature in PLE. Each distinct peak in this PL/PLE map corresponds to the photoexcitation of excitons in the second subband, E_{22}, (absorption in visible range) followed by the recombination of excitons in the first subband, E_{11}, (near-infrared emission). These transitions can be resolved for each (n, m) type due to significant splitting of either E_{11} or E_{22} energies, or both, shown as vertical and horizontal hairlines correspondingly. This particular sample included predominately (6,5) SWNTs, which is typical feature of the CoMoCat product. The strongest PL peak at 994 nm seen in Fig.1.4 corresponds to the emission from the bright excitons in the lowest subband of (6, 5) SWNTs. Correspondingly, as a function of the photoexcitation energy, the PL intensity reaches a maximum at an excitation wavelength of about 570 nm where the excitation is in resonance with the E_{22} excitonic subband. The structure of the peaks, both in PL and PLE, also includes smaller broad features which can be assigned to the phonon-assisted processes.

1.4 Radiative and nonradiative lifetimes of excitons

The luminescence properties of semiconducting SWNTs have attracted much attention over the past decade. The exciton radiative lifetime τ_r can be estimated from the PL quantum yield (QY) η_{PL} and the effective PL decay time as

$$\tau_r = \frac{\tau_{PL}}{\eta_{PL}}$$

where η_{PL} is defined as

$$\eta_{PL} = \int_0^\infty \frac{I(t)}{I(0)} dt$$

from the time-dependent PL curve $I(t)$. Note, that τ_{PL} defined here is not the averaged lifetime in general. It is though a useful empirical quantity proportional to the steady-state PL intensity.

Despite a number of experimental and theoretical studies of τ_r in SWNTs, the range of reported values of τ_r is wide: from 10 to 100 ns, presumably because of the

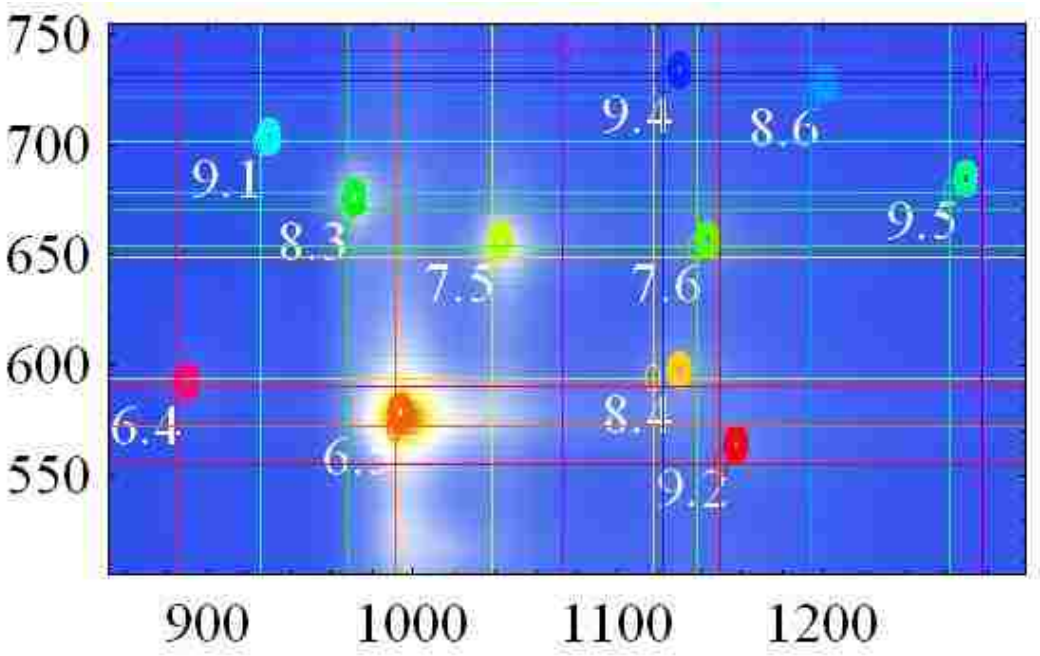

Figure 1.4: PL/PLE map of SWNT/DNA solution

variation of the experimentally determined η_{PL}, as well as due to varying quality of the samples. The QY varies much, depending on the amount of residual bundles, graphitic impurities, etc. For example in surfactant-suspended SWNTs QY=0.01% $\div$ 1%.

Early PL measurements of SWNT QY in solutions reported discouragingly small values on the order of $10^{-4} - 10^{-3}$, implying that nonradiative processes in such samples outweigh the radiative decay. Recent studies report on the measurements of exciton lifetime approaching the radiative lifetime in high-quality nanotube ensembles. Relatively high $\eta_{PL} > 1\%$ was measured for highly isolated nanotubes using such polymer wrapping as PFO [37] and sorting and purification of SWNTs by density gradient ultracentrifugation. Different group reports about 8% or even

20% QYs [34,38,39]. From such purified SWNTs, the PL lifetimes and QYs can be measured with sufficient accuracy to estimate the radiative lifetime.

Nonradiative lifetime depends on many factors. Efficient PL quenching happens at the tube ends, which act as exciton sinks [40]. In a recent study, using suspensions of length selected SWNTs, it was shown that an increase of PL QY occurs for a tube length above 1μm. This characteristic length is explained by comparing the (length independent) quenching rate along the tube, $1/\tau_{PL}^{\infty}$, with the probability of an exciton to diffuse to the tube ends and recombine there with the rate $1/\tau_{nr}^{end} \simeq 1/20ps^{-1}$.

Fitting a 1D diffusion model to experimental data, the exciton diffusion constant, $D = 0.4cm^2/s$, and the asymptotic PL lifetime for infinitely long tubes, $\tau_{PL}^{\infty} = 50 \div 100ps$, were estimated in [41].

Other mechanisms describing nonradiative decay of SWNT excitons will be further discussed in Chapter 4.

1.5 Influence of SWNT environment on exciton energy levels

The energies of the optical transition (of SWNT excitons) are strongly affected by changes of dielectric environment of SWNTs. For example, the dielectric screening introduced by bundling, surfactant molecules, DNA or polymer wrapping, etc. may shift the position of PL lines [8, 26, 42, 43]. Historically, first reliable PL measurements resolving SWNTs of individual chiralities were done in SWNT solutions/surfactant suspensions. The transition energies of SWNTs individually suspended in air or vacuum are usually blue-shifted compared to those in water and/or various dielectric media. This blue shift presumably reflects the degree of surfactant coverage and its polarizability. Such a surfactant dependent variation of the dielectric screening influences Coulomb interactions between electron and hole in SWNTs. A shift of the exciton energy vs. the dielectric constant can be used to estimate the scale of the binding energy itself. Bundling of SWNTs causes a red

shift of the exciton energy due to dielectric screening by the adjacent SWNTs.

This dependence of the exciton energy shift on the dielectric constant of the surrounding media was studied in Refs. [44, 45]. As the dielectric constant of the surrounding material increases, the red shift of the E_{11} exciton energy increases in comparison with individual SWNTs suspended in vacuum. The screening effect can be attributed to the combination of the screening of the charge carriers in the nanotube itself and in the surrounding medium. In order to establish how the exciton energy depends on the macroscopic dielectric constant of the surrounding media, the Bethe–Salpeter equation must be solved [46]. The calculation within the effective medium model without frequency dispersion of dielectric function qualitatively reproduces the experimentally observed relationship between the transition energy and dielectric constant for SWNTs over a range of chiral indices (n, m). The results show that environmental effects depend not only on the dielectric constant of the media but also on the diameter and chiral angle of SWNTs (n, m). It has also been theoretically pointed out that the red shifts of the optical transition (exciton energy) mostly results from the polarizability of the attached physisorbates on a SWNT, suggesting the importance of a microscopic understanding of the screening effect [47]. In our group a theoretical model of the exciton binding for the charge impurities in the medium has been developed [48].

The screening effects caused by SWNT doping, that is, by additional free charge carriers, and changes in the optical transition energies following from this were also studied. This effect was theoretically predicted [49] and experimentally studied using single nanotube devices where the carrier density (Fermi energy) was tuned by electrostatic gating [50].

1.6 Förster Resonance Energy Transfer (FRET)

Förster Resonance Energy Transfer (FRET) is a process of non-radiative energy transfer between an excited state of a donor and a ground state of an acceptor. The original theory by Förster is based on dipole coupling.

While the primary equations for FRET are based on the interactions of non-overlapping transition dipoles, other mechanism of coupling are possible. For example, the energy transfer was found between species with significantly overlapped wavefunctions. It is usually described in terms of Dexter theory [51], where the coupling decays with distance exponentially.

The first theoretical formulation was made by Förster [52] who predicted that the effect scales as an inverse sixth power of the distance between the species. It was experimentally verified by Latt et al. [53]. Consider the transfer of excitation between the donor **A** and the acceptor **B**. Assume, that the excitation generates an electronic excited state of a donor, **A***, followed by decay to the ground electronic state. At the same time the state **A*** can be mixed with the acceptor state **B*** which means it undergoes a transition from its ground to excited state. The excited acceptor **B*** subsequently radiatively decays to the ground state.

The Förster theory gives the following expression for the rate of energy transfer w_F, for systems where the host media for donor and acceptor (solvent) has the refractive index n:

$$w_{AB} = \frac{9k^2c^4}{8\pi\tau_{A*}n^4R^6}\int F_A(\omega)\sigma_B(\omega)\frac{d\omega}{\omega^4}. \tag{1.2}$$

In this expression, F_A is the PL spectrum of the donor (normalized to unity); τ_{A*} is the associated radiative lifetime (related to the measured PL lifetime τ_{PL} through the PL quantum yield $\eta = \tau_{PL}/\tau_{A*}$); σ_B is the linear absorption cross-section of the acceptor; and c is the speed of light. The k factor depends on the orientations of A and B dipoles with respect to each other and with respect to their mutual displacement unit vector $\hat{\mathbf{R}}$ as follows:

$$k = (\hat{\mu}_a \cdot \hat{\mu}_b) - 3(\hat{\mathbf{R}} \cdot \hat{\mu}_\mathbf{a})(\hat{\mathbf{R}} \cdot \hat{\mu}_\mathbf{b}). \tag{1.3}$$

$\hat{\mu}$ designates a unit vector in the direction of the appropriate transition dipole moment. The magnitudes of the transition matrix elements (electric dipole moments) for the donor decay and acceptor excitation are:

$$\mu_A = \langle\Psi_A|\mu|\Psi_{A*}\rangle; \qquad \mu_B = \langle\Psi_{B*}|\mu|\Psi_B\rangle, \tag{1.4}$$

where the μ is the dipole operator. Comparing the above results reveals the operator for the interaction of two static dipoles:

$$\frac{\mu_A \mu_B}{4\pi\epsilon_0 R^3}\left[(\hat{\mu}_a \cdot \hat{\mu}_b) - 3(\hat{\mathbf{R}} \cdot \hat{\mu}_{\mathbf{a}})(\hat{\mathbf{R}} \cdot \hat{\mu}_{\mathbf{b}})\right], \tag{1.5}$$

in the transfer rate equation. However, since it is an off-diagonal matrix element connecting different initial and final states, the final expression must include it in the second order, finally giving the required $1/R^6$ dependence. The k factor appearing in the theoretical consideration here, in practice, is often replaced by $k^2 = 2/3$ for isotropic media.

In experimental study, it is convenient to introduce the concept of a critical distance R_0, as a separation at which the theoretical rates of FRET and spontaneous emission by the donor are equal (now known as the Förster distance). Then the expression for the rate of energy transfer becomes simpler:

$$w_F = \frac{1}{\tau_{A*}}\left(\frac{R_0}{R}\right)^6. \tag{1.6}$$

and the efficiency of the Förster energy transfer is:

$$W = \frac{1}{1 + (R/R_0)^6}. \tag{1.7}$$

FRET can be determined by using both steady-state and time-resolved methods. For example, in the steady-state, the relation between FRET efficiency and PL intensity with and without an acceptor is:

$$W = 1 - \frac{I_{AB}}{I_A}. \tag{1.8}$$

The relation between the PL lifetime of donor, PL lifetime of donor in presence of acceptor, and FRET efficiency is:

$$W = 1 - \frac{\tau_{AB}}{\tau_A}. \tag{1.9}$$

Förster Resonance Energy Transfer was found to be useful tool to study interactions in nano-scale complexes. Experimental results using this technique will be presented in Chapter 2.

Thesis outline

This thesis is organized as follows:

- Chapter 2 studies the SWNT/DNA/REI complexes by using Resonant Energy transfer. The spatial correlation analysis will provide additional evidence of such complex formation.

- Chapter 3 focuses on the behavior of terbium ions themselves in the crowded environment of SWNT hydrogel. The time-resolved and steady-state spectroscopy data provide useful information about screening of terbium ions from the water molecules.

- Chapter 4 discusses the interaction inside of SWNT/DNA hybrid under two-color wavelength excitation.

Chapter 2

Energy transfer between SWNT/DNA and Rare Earth Ions due to their spatial correlations

In this chapter we will discuss two different sets of energy transfer measurements: (1) between unlike REIs, Tb^{+3} and Eu^{+3}, and (2) between SWNTs and each of these REIs, using previous results as calibration. $EuCl_3$ and $TbCl_3$ REI salts dissolved in deionized (DI) water were used for the sample preparation, and solution of SWNTs wrapped with single-stranded DNA (ssDNA) was prepared from "as produced" CoMoCat material and $(GT)_{20}$ DNA. Original solution of SWNT wrapped with the ssDNA was centrifuged using filter, and re-suspended in DI water with an appropriate concentration to remove completely the trace of the original buffer. This procedure is similar to that described in the paper [28]. After establishing a reliable calibration for the energy transfer distance in Tb-Eu solution, next the spatial correlation between SWNT and REIs is studied as a function of the concentration of the species.

The energy transfer process requires two probes: a donor and an acceptor. Its mechanism is based on the dipole interaction between an excited state of a donor and a ground state of the acceptor atom/molecule, resulting in exchange of the

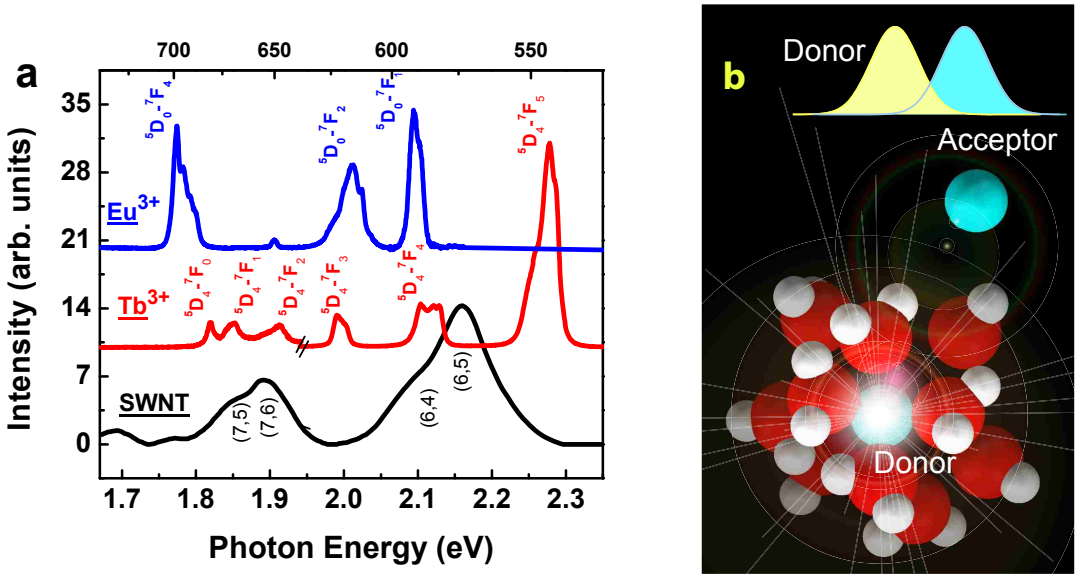

Figure 2.1: (a) Superimposed PL spectra of REI in solution: pure Tb^{3+} emission (red curve) at 488 nm wavelength excitation, pure Eu^{3+} emission (blue curve) at 514 nm wavelength excitation, and SWNT optical absorption spectrum (black line). The baselines were offset for clarity. (b) Sketch of the first coordination sphere of a solvated REI, surrounded with the partially oriented water molecules and spatially isolated from another ion. Inset shows that for efficient FRET between the ions, a strong spectral line overlap is required, in addition to the short distance.

excitation between the molecules. The probability of this process can be related to the matrix element of interaction, H_{int}, and the optical densities of the donor and acceptor molecules. We will use an abbreviation "FRET", which means *Fluorescence (or Förster) Resonance Energy Transfer* for resonance energy transfer, although it may include also components of exchange beyond the dipole-dipole approximation, as was shown by Dexter [51]. The overall transfer rate, w_{AB}, depends on the mutual spectral overlap, Ω, between the line shape functions of the optical transitions, $g_A(h\nu)$ and $g_B(h\nu)$. Existence of FRET requires an appreciable overlap between the spectral lines of the emitting and receiving species, as follows from:

$$w_{AB} = \frac{(2\pi)^2}{h} |\langle A^*B|H_{int}|AB^*\rangle|^2 \int g_A(h\nu)g_B(h\nu)d(h\nu), \qquad (2.1)$$

where ν is the frequency, h is the Planck constant and H_{int} is the interaction Hamiltonian.

A unique characteristic of the trivalent rare-earth ions is that the electron-phonon coupling is very weak for all optical transitions which take place within the 4f manifold (all transitions that we study). I.e., no Stocks shift between the emission and photoexcitation spectra is expected. Therefore, the line shape of the radiative transition is approximately the same as for the reciprocate transition (absorption line). Thus we can use our PL data only to calculate the spectral overlap functions.

Steady-state photoluminescence (PL) of REI solutions is presented in Fig.2.1a. The energy of transitions can be compared to the energies of transitions in the single ion. The significant broadening is likely due to the interaction with the water solvation shells of the ion (schematically shown in Fig.2.1b). REI is known to form a complex with 8 or 9 water molecules in solution (Fig.2.1b), and there exist even longer correlations, beyond this first water solvation shell. Fine structure of the spectral lines is reproducible. Final assignment of the spectral lines and corresponding transitions between energy levels can be found in Fig. 2.1a and 2.3a respectively.

The overlap of two spectra allows one to evaluate the FRET between Tb and Eu. Numerical convolution of the area under the curves gives an appreciable overlap between the spectra of Tb and Eu ions in the energy region 1.75-2.35 eV (Fig. 2.2d).

2.1 Time resolved spectroscopy

Within the Förster model, [51, 52] the temporal variation of the emission of the sensitizer (donor) must shorten due to the activator (acceptor). The magnitude of the transfer efficiency is given by:

$$W = 1 - \frac{\tau_A^B}{\tau_A^0}, \tag{2.2}$$

where τ_A^B and τ_A^0 are the decay time of the sensitizer A in the presence of the activator B, and the radiative lifetime of the pure sensitizer, respectively. Time-resolved

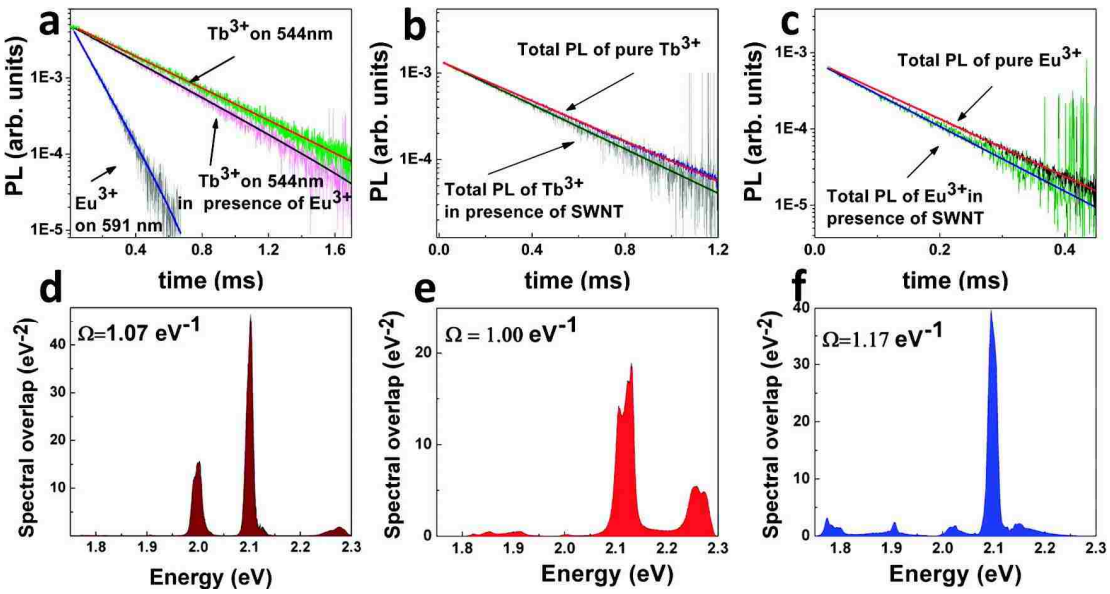

Figure 2.2: Time-resolved PL for (a) pure REIs and their mixed solution, (b) pure Tb and Tb-SWNT mixed solution and (c) pure Eu and Eu-SWNT mixed solution. Spectral overlaps for (d) Tb with Eu, (e) SWNTs with Tb, and (f) SWNTs with Eu.

spectroscopy following pulse laser excitation of selectively (resonantly) excited Tb^{3+} ions in the $TbCl_3$ water solution showed a typical PL lifetime of $\tau_{Tb}^0 \approx 0.395ms$. In the mixed solution which contained both Tb^{3+} and Eu^{3+} ions we observed systematic shortening of Tb decay time: $\tau_{Tb}^{Eu} \approx 0.366ms$.

Shortening of the PL lifetime may be attributed to the increase of radiative and/or non-radiative rates. The increase of the radiative rate can be rejected because we did not observe an increase of the PL efficiency, which would result from a faster radiative recombination. Increase of the non-radiative rate is possible, in principle.

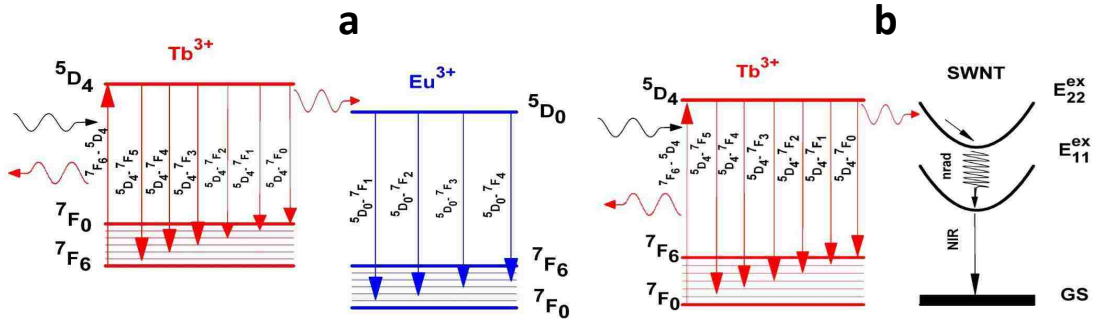

Figure 2.3: FRET energy level diagram: a) between Tb and Eu ions, b) between Tb and SWNT.

It may be due to a strong interaction with the polar water molecules. However, this interaction with water is present even in the pure solution where the REIs are surrounded by solvation shells (Fig. 2.1b). The coupling is unlikely to strengthen in the mixed solution where the solvation shell may become only distorted. In fact it was observed earlier that the non-radiative decay rate becomes lower when REI-water solvation structure is influenced by another substance [54]. Then we have to assume an additional non-radiative channel to appear which can be FRET. Fig. 2.2a shows shortening of Tb lifetime for 544nm $^5D_4 \longrightarrow ^7 F_5$ transition in the presence of Eu (pink curve) compared to original decay in the pure Tb solution (black curve). In case of Tb^{3+}/Eu^{3+} system shown in Fig. 2.2a, the corresponding transfer efficiency is about 7%.

2.2 FRET mediated acceptor emission

If the shortening of decay time in Fig. 2.2a is due to FRET between Tb and Eu one should be able to verify it by measuring the induced PL. Indeed, in Fig.2.4 the direct observation of the energy transfer by steady state PL spectroscopy is presented. The mixed solution was excited selectively at the wavelength 488 nm which fits only Tb^{3+} ion and does not fit any excitation line for the Eu^{3+} ion. The FRET-mediated emission line $^5D_0 \longrightarrow ^7 F_4$ from the Eu^{3+} is evident in the spectra

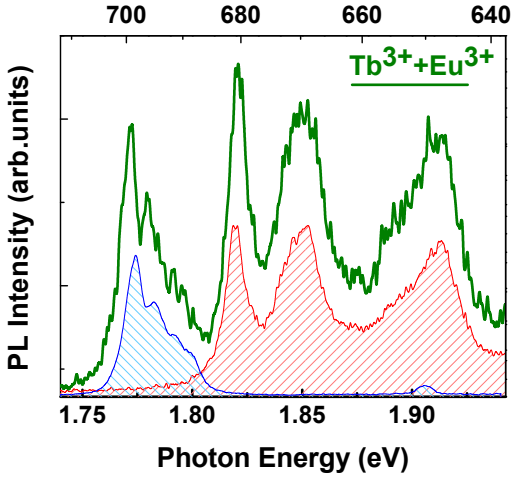

Figure 2.4: PL emission of the mixed solution containing both REIs (green curve) at 488 nm excitation (Tb resonant wavelength excitation). The transfer-mediated emission line from Eu^{3+} at 699 nm is superimposed with the PL emission of solution of pure Tb (red) or pure Eu (blue), excited at 488 or 514 nm, respectively.

at $h\nu = 1.77eV$ ($\lambda = 699$ nm). For comparison, on the same graph we present the PL spectra of the pure Tb solution (red curve) showing no PL in the same range (the spectral lines of Tb^{3+} emission are seen above 1.8 eV) and the pure Eu solution (blue curve), demonstrating the same band ${}^5D_0 \longrightarrow {}^7F_4$ for Eu^{3+} transition. The FRET energy level diagram for Eu and Tb ions is shown in Fig.2.3a.

Given this qualitative confirmation of the FRET, we were further able to provide a quantitative estimate via the spectral weights of the PL bands of Tb and Eu. Fitting the PL intensity of the mixed solution (green curve in Fig.2.4) with the weighted PL spectra of the pure solutions (red and blue curves) we obtained partial contributions of the REIs. Taking into account that the concentrations of Tb and Eu were the same in the mixed solution but the quantum efficiency of Eu is slightly lower, as detailed in next section, and assuming a lossless internal conversion of the transferred energy into ${}^5D_0 \longrightarrow {}^7F_4$ radiative transition, we estimated from the above the FRET-induced PL efficiency to be $\approx 10\%$, comparable with the one

obtained from the life-time shortening.

2.2.1 Calculation of the Quantum Yield of the REIs solutions

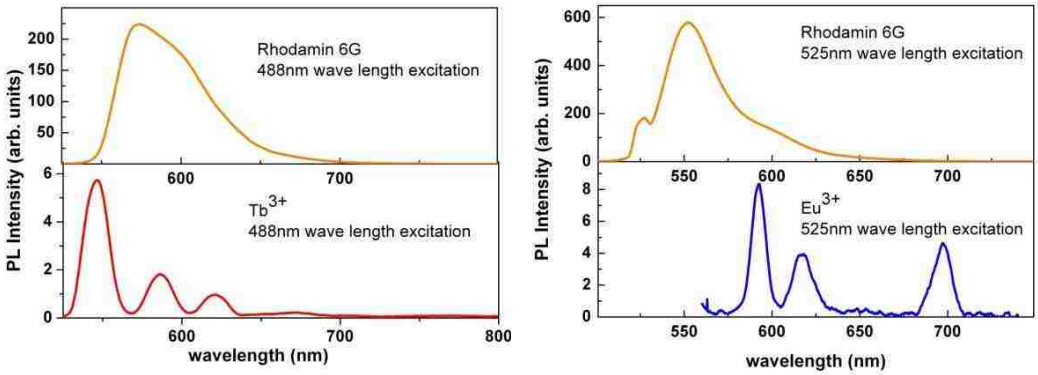

Figure 2.5: PL spectra for Rhodamine 6G (upper left, and upper right); for $EuCl_3$ (lower right), and $TbCl_3$ (lower left) solutions. The excitation wavelength is 488nm (left) and 525nm (right).

The PL quantum yields of Tb and Eu ions are determined as the ratio of the total luminescence intensity to the intensity of absorbed radiation. To calibrate the PL spectra, we used the sample with the known PL quantum yield. For this purpose an ethanol solution of Rhodamine 6G was chosen where the nominal quantum yield is close to 100%. This Rhodamin sample has been diluted until PL intensity became linear with the concentration of Rhodamin in solution (the original solution showed a saturation of the PL). The quantum yield of the REI solution was calculated as:

$$\eta_{REI} = \eta_{Rh} \frac{\int I_{REI}(\lambda) d\lambda}{\int I_{Rh}(\lambda) d\lambda} \frac{A_{Rh}}{A_{REI}} \tag{2.3}$$

where I_{REI} and I_{Rh} are the PL intensities of REI and Rhodamin 6G in solution (integrated in the range of the corresponding spectral lines); A_{REI} and A_{Rh} are

Table 2.1: The data used to calculate the REI quantum yields: $\eta_{Tb} = 1.3\%$ and $\eta_{Eu} = 0.8\%$.

	REI integrated PL intensity (arb. units)	Rh integrated PL intensity (arb. units)	REI Absorption	Rh Absorption	Quantum Yield %
Tb	176.32	14186.21	2.6×10^{-3}	2.9×10^{-3}	1.3
Eu	232.83	26310.06	1×10^{-3}	1.1×10^{-3}	0.8

the absorption coefficients of the REI and Rhodamine 6G at the wavelength corresponding to the REI resonant excitation (which is 488 nm for Tb and 525 nm for Eu). In the PL measurements 20 ps tunable laser (at 2 mW power) was used as the excitation source. Ocean Optics spectrometer USB2000 with a 2048-element Toshiba linear CCD array was used for acquisition of the emission spectra for both Rhodamin, and Tb and Eu. The results are summarized in Fig.2.5. We estimate the error in calculation of the QY to be $\approx \pm 15\%$ for Tb and $\pm$ 20% for Eu.

Absorption spectra were taken with a Perkin Elmer Lambda 2 Spectrophotometer. Fig.2.6 presents the absorption data for all species.

2.3 FRET in REI-SWNT samples

Using REIs as a reference for the calibration, next we measured the shortening of Tb and Eu emission in the presence of ssDNA/SWNT. Indeed, decay times of most of the REI lines demonstrate similar substantial shortening as an indication of the FRET from a REI to the SWNT. The emission data for the mixed solution was collected both through the monochromator and without it to measure the FRET at the wavelength corresponding to the peak of emission or the total PL intensity of the donor. The lifetime shortening was almost the same for all of the REI PL bands. Thus we present in Fig.2.2b the decay time of the total PL from the pure Tb and from the mixed solutions of Tb/SWNT (at the resonant wavelength excitation

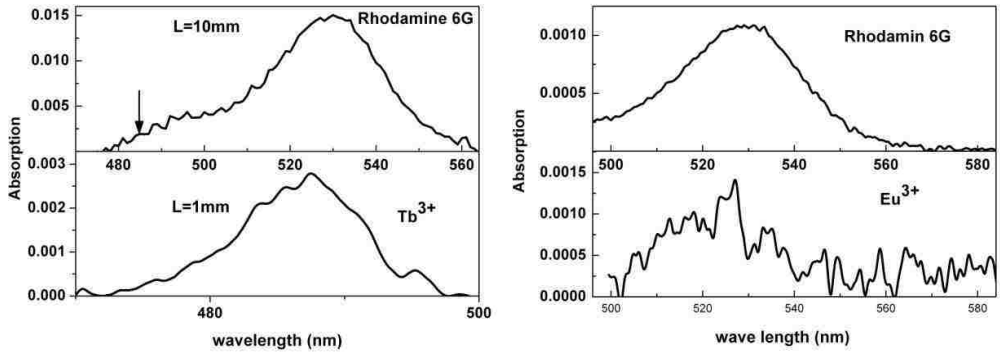

Figure 2.6: Absorption spectra for Rhodamine 6G (upper left, 10 mm cell, and upper right, 1 mm cell); for $TbCl_3$ (lower left) and $EuCl_3$ (lower right) solutions.

for Tb). The SWNT concentration was 4 mg/L. Fig.2.2c shows corresponding data for pure Eu and Eu/SWNT (at 525 nm, the resonant wavelength excitation for Eu). The decay time shortening corresponds to the FRET transfer efficiency of 10% and 7% for Tb and Eu respectively. The magnitudes of Ω in Fig.2.2e,f are also comparable with the spectral overlap between Tb and Eu in Fig.2.2d.

Even though the same energy transfer mechanism as in Sec. 2.2 is responsible for PL lifetime shortening in the REI/SWNT solution, one cannot observe FRET-induced PL from the SWNTs in the visible range. This is due to the SWNT charge carriers, after excitation in the second subband, E_{22}^{ex}, experience a fast non-radiative inter-subband relaxation into the lowest subband, E_{11}^{ex}, during 10-20 ps (Fig.2.3b), followed by a longer radiative and non-radiative relaxation to the ground state [55]. Thus the efficiency of SWNT PL in the visible range, E_{22}^{ex}, is negligible small. We were able to observe SWNT infra-red emission from the E_{11}^{ex} levels in a separate set of experiments.

Figure 2.7 shows PL spectra of the mixed solution with $TbCl_3$ (red) compared with the PL from the pure SWNT/DNA solution (blue, normalized to the main (6,5) peak intensity). Three extra PL peaks are evident, which we attribute to the

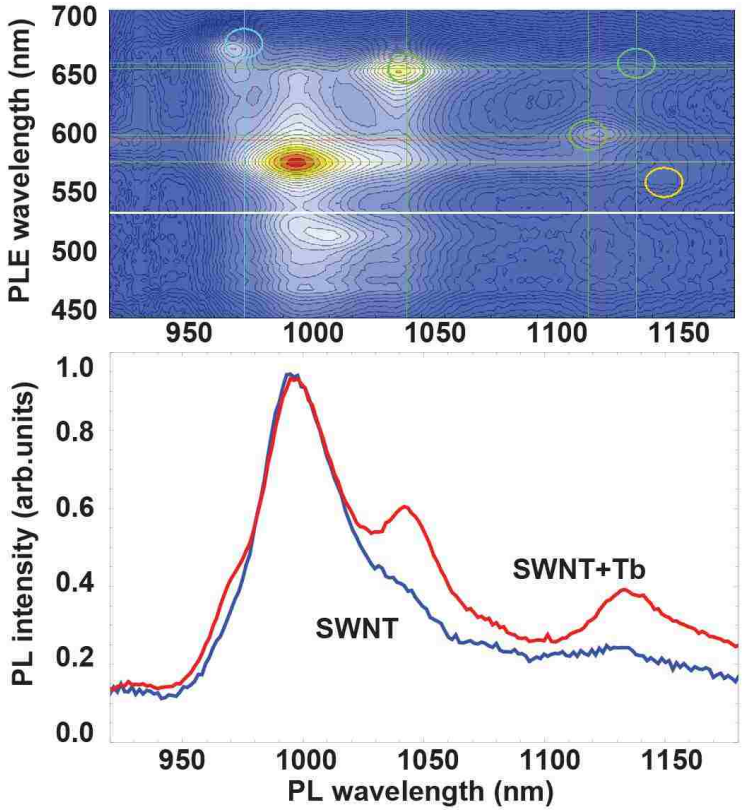

Figure 2.7: PL (blue) and FRET-induced PL (red) emission of the SWNT/DNA solution (mainframe). (Upper inset) PL/PLE map of the pure SWNT solution with thin lines and circles denoting separate chiralities, following the literature data. White line corresponds to the PL (blue curve in the mainframe) at the Tb resonant wavelength excitation at 532 nm (2.33 eV). The PL FRET-induced emission of several SWNTs that cannot be resonantly excited at 532 nm is clearly seen as 3 peaks on the PL from the mixed solution (red curve).

transfer-mediated emission from (8,3), (7,5), and (7,6) SWNTs at 968, 1038, and 1138 nm, respectively, using our absorption data (see section Near infra-red (NIR) absorption of the pure SWNT/DNA solution) as well as the PL/PLE map shown in the upper inset of Fig.2.7.

2.4 Spatial correlation analysis

The time-resolved measurements were repeated for solutions with different relative concentration of REIs and SWNT. In Fig.2.8 representative data were plotted for increasing SWNT content in the mixed solution, from left to right. Black squares/triangles correspond to concentrated solution of pure terbium/europium: $[SWNT] = 0$, $[Tb]$; or $[Eu] \approx 1.2M$. Upon adding SWNTs to the pure solution significant decrease of the lifetime but also large scatter of the data were observed (red circles and blue triangles in Fig.2.8a for Tb and purple pentagons for Eu in Fig.2.8b). The scattering can be attributed to the fact that the sample is not uniform anymore.

We propose this overall lifetime shortening should be explained by the formation of physical complexes of REI and SWNTs in solution. Indeed REI and SWNT have opposite charges in solution. The ionization of the DNA backbone results in a significant negative total surface charge density of the SWNT/DNA hybrid. Positive REIs should be attracted by this negatively charged surface. Thus the pair-correlation function for the REI (as a donor) and SWNT (as an acceptor) should be greatly enhanced, as compared to the non-interacting species. We stress that these solutions with the low SWNT content still contain REIs in excess. The SWNT/DNA surface charge is fully compensated and only a fraction of REIs is bound. Significant amount of Tb/Eu ions is in its free (solvated) state. We excited and probed the solution in confocal geometry. Within the focus area of our setup the solution became non-uniform after adding REI, possibly due to the SWNT coalescence. Thus, in different measurements we were able to probe either the volumes that contain more REI bound to the SWNT/DNA surface or those where the free REI ions dominate the PL response. Thus one should observe a distribution of the lifetimes with two limiting values, given by fully solvated (free) REIs and by partially correlated (bound) REIs.

The first measurements already indicated the existence of two different lifetimes in the solution, due to free and bound REIs. Even though additional experiments

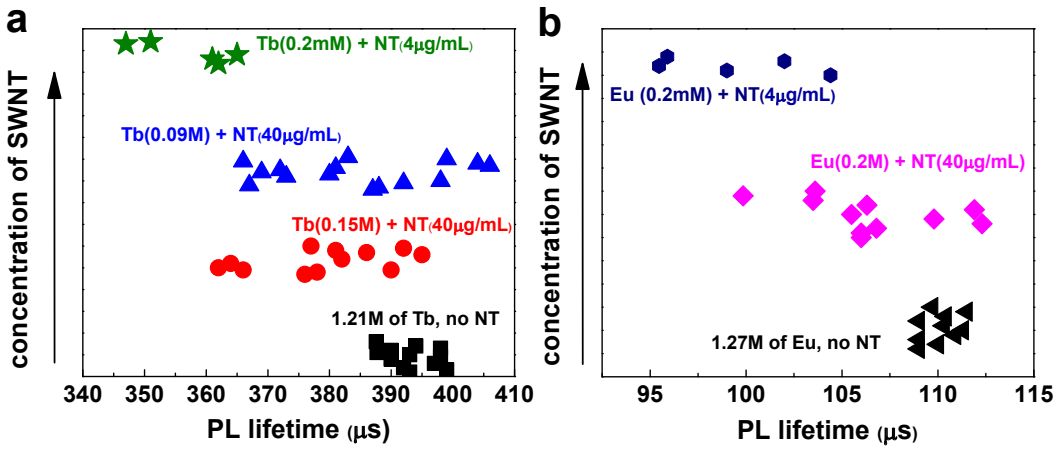

Figure 2.8: a) PL lifetime of the pure Tb solution and the SWNT mixed solution as a function of relative concentration of SWNT (activator). b) Same for Eu.

were designed with the higher relative concentration of SWNTs. For example, solution with $[Tb] = 0.14 - 0.2mM$ and $[SWNT] = 4mg/L$ has showed single PL decay time (green stars in Fig.2.8a) which was attributed to Tb-SWNT/DNA complex only. We speculate that these samples had a concentration of Tb corresponding or close) to the saturation of the charge of the DNA/SWNT, estimated from the DNA backbone charge density (the linear charge density of the DNA-NT hybrid is -6 $\bar{e}/nm$ [56]). The observed difference between free Tb PL lifetime (black symbols), $0.395 \pm 0.005ms$, and the one in the complex (green stars), $0.350 \pm 0.005ms$, gives the 10% FRET efficiency. Very similar results for Eu bound to SWNT/DNA in the mixed solution with $[Eu] = 0.2mM$ and $[SWNT] = 4mg/L$ has showed FRET efficiency 7% (dark blue diamonds in Fig.2.8b). We emphasize that in REI-SWNT system, upon lowering the concentration of the REI sensitizer by more than three orders of magnitude as compared to the set of experiments with the unlike REIs, the FRET not only remains observable but also its efficiency persists at the same level, which cannot be expected for simple non-interacting solution.

The extraordinary high FRET efficiency (for relatively low concentration of the SWNT activator) requires additional attention. Another essential parameter of the

energy transfer is the critical distance, R_c. The transfer efficiency can be expressed as:

$$W = \frac{1}{1 + \frac{R^6}{R_c^6}}, \tag{2.4}$$

where R is the distance between emitting and receiving species, R_c is the Förster distance when the efficiency of the FRET is 50%. This distance depends on the optical parameters of the system as [57]:

$$R_c = \left(\frac{3 f_B \, h\Omega \, \eta_A \, e^2}{4k^4 \, n^4 \, 4\pi \, \epsilon_0 \, mc} \right)^{1/6}, \tag{2.5}$$

here Ω is the spectral overlap, ϵ_0 is the vacuum permittivity, e and m are the electron charge and mass, c is the speed of light and h is the Planck constant, η_A is the quantum yield of PL of the sensitizer, f_B is the oscillator strength of the receiving species (SWNT or Eu ion) at the wavevector $k = \omega/c$, and the angular resonance excitation frequency is $\omega = 2\pi\nu$. The Förster distance for Eu is known: $R_c \approx 10$Å(an average value taken from the literature [58, 59]). For SWNT this distance can be evaluated *via* the oscillator strength:

$$f_{SWNT} = \frac{2\epsilon_0 \, mc}{\pi e^2} \frac{9n}{(n^2+2)^2} \sigma(\omega)\Delta\omega, \tag{2.6}$$

where the refractive index is taken to be $n = 1.4$ for the water solution, $\sigma(\omega)\Delta\omega$ is the acceptor absorption cross section times the bandwidth of the transition. Considering that the average absorption cross section of a SWNT is $\sigma \approx (0.73 \div 1.8) \times 10^{-17} cm^2/atom$ (literature values from refs. [35,36,39,60]), and $\Delta\omega \approx 30meV$ (fit to our data) we estimate the SWNT average oscillator strength to be $(1.6 \div 3.95) \times 10^{-3}$, which is consistent with previous studies. In the most resent work [61] the oscillator strength was measured for E_{22} exciton: 6×10^{-3}.

The PL quantum yield of REI sensitizers was experimentally measured: $\eta_{Tb} = 1.3\%$ and $\eta_{Eu} = 0.8\%$ which are the typical values for REI water solutions [62]. Using these results $R_c \approx 10.9 \pm 0.8$ Åfor Tb/SWNT solutions and $R_c \approx 10.4 \pm 0.8$Å for Eu/SWNT solutions were derived. Note, that despite the uncertainty in f_{SWNT},

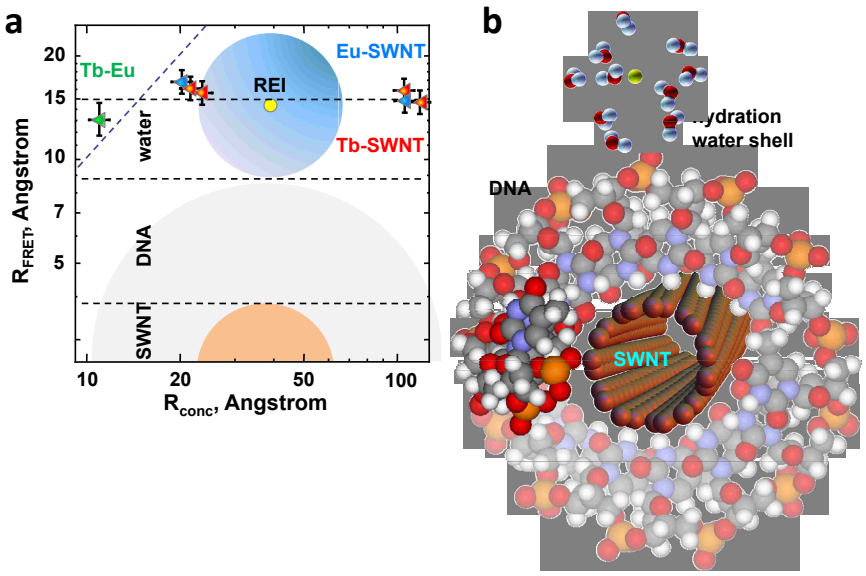

Figure 2.9: Cross-correlation plot of the sensitizer-activator critical distance as determined from the FRET vs. the distance derived from the concentration of the species (double logarithmic scale). Dashed diagonal line shows the cross-correlation for the non-interacting components, dashed horizontal lines represent SWNT, DNA and water shell excluded volumes from bottom to top. The image shows geometry of the complex.

due to the averaging over the SWNT ensemble and relatively large range of σ, the Förster distance can not substantially change because it has weak (power of 1/6) dependence on the materials' optical parameters according to the equation above.

Following this simple calculation we obtain an estimate for $R \approx 14 \pm 2$Å for FRET in Tb-Eu system. On the other hand, in $TbCl_3$ and $EuCl_3$ solutions with the concentration $c = 1.2M$, the minimum distance between unlike REIs in the mixed solution is approximately 11Å. This number is in a good agreement with the one obtained from the FRET efficiency between Tb and Eu.

One can plot the FRET distance between the donor and acceptor vs. the "physical distance" evaluated from the concentration of the donors and acceptors (REIs,

SWNTs). Naively, within experimental accuracy, these two distances should be the same. That is the distance-distance correlation plot should show straight diagonal line (dashed line in Fig.2.9). In fact, the REIs showed a negative correlation due to the Coulomb repulsion between positively charged ions, that is, a smaller FRET efficiency than the one expected for an ideal non-interacting solution. Indeed the Tb-Eu data point (green triangle in Fig.2.9), averaged over multiple measurements of the FRET efficiency, is above the dashed diagonal line corresponding to the non-interacting components.

The nominal distance between the species for Tb/SWNT and Eu/SWNT solutions obtained from their concentrations, R_{conc}, is an order of magnitude larger than for the Tb-Eu case. Even though we measured very strong FRET signal which corresponds to the average critical distance for REI-SWNT case $R \approx 14.6 - 17.2$Å, plotted on the vertical axis in Fig.2.9. Thus the data points for Tb-SWNT (red) and Eu-SWNT (blue) solutions are well below the diagonal dashed line for the non-interacting components. We speculate that this is possible only in the case of formation of REI-SWNT complexes due to the electrostatic attraction between the negatively charged DNA backbone (ionized phosphate groups) and positively charged REIs in the water solution. Similar interaction is known to result in a fast ion condensation on the surface of the DNA rods [63, 64], changing the ion pair correlation function, significantly reducing the spacing and making the FRET possible.

The obtained value for R is in agreement with the proposed geometrical size of the complex, shown as a background and on the right side of Fig.2.9. The radius of the SWNT/DNA hybrid is expected to be ∼9–11 Å. The DNA thickness ≈5.1 Å (from [27]) and the REIs solvation shell width should be added. The first coordination sphere of the solvation water molecules is at ∼2.5 Å for typical REIs, and it is at ∼4.5 Å for the second coordination sphere. Thus the critical distance evaluated from the exclusion volume argument (dashed horizontal line in Fig. 2.9) is consistent with the measured one from the FRET and is much smaller than the distance between the non-interacting species from the known concentrations of initial solutions (dashed diagonal line).

2.5 Appendix

2.5.1 Near infra-red (NIR) absorption of the pure SWNT/DNA solution

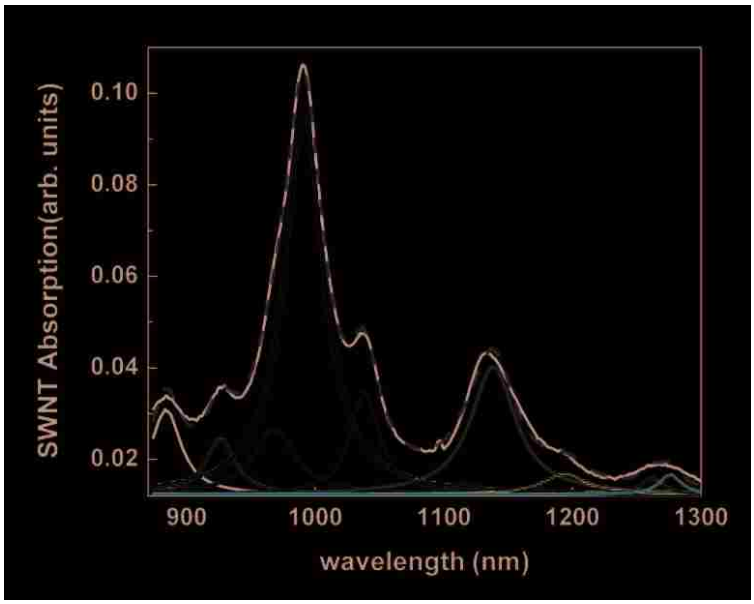

Figure 2.10: NIR absorption of the SWNT/DNA DI water solution: (black solid line) total absorption experimental data, (green dashed line) cumulative model fit, (color lorentzians) partial SWNT contributions as listed in Table 2.1.

A simple Lorentzian shape with a FWHM $\approx$ 0.03eV was used for NIR spectra fitting to determine the peak positions of E_{11} optical transitions. Analysis of the absorption data for SWNT/DNA solution is based on the previously reported values from X.Tu et al. [27] In this work the absorption data was taken from similarly prepared DNA wrapped SWNTs, which allows the most reliable peak assignment. We have observed only minor shifts ($\sim$ 1-3 nm) of the SWNT peaks in our sample. We assigned amplitudes for 10 different SWNT species, listed in the Table.

Table 2.2: NIR absorption analysis of SWNT/DNA sample.

SWNT chirality (n,m)	E_{11}, nm	Amplitude, arb. un.
(6,4)	884	0.82
(9,1)	926	0.53
(8,3)	968	0.89
(6,5)	991	4.77
(7,5)	1038	0.93
(9,4)	1122	0.07
(7,6)	1138	1.84
(8,6)	1194	0.28
(9,5)	1262	0.11
(10,5)	1276	0.14

2.5.2 Stability of nano-complex

Here we provide evidence for the stability of the nano-complex outside the solution.

The REI/DNA/SWNT solution was evaporated. The residue, including the complexes, was collected on a sapphire or silica substrate for photoemission study to prove the ionization states of the RE ions. Twin samples have been prepared from the $TbCl_3$ salt solution without SWNTs. Dried REI samples have been investigated with the high-resolution XPS using the Scienta ESCA-300 spectrometer (see Fig.2.11). The XPS 4d core-level spectra of Tb with and without DNA/SWNT show maxima at 151.7 and 153.5 eV, respectively (Fig.2.11). The peak at 153.5 eV is characteristic for the Tb^{3+} ionization state, as expected for pure REI salts. The

change of the shape of the peak (decrease of the high binding energy component) confirms an increased concentration of Tb ions with the lower oxidation number than in the $TbCl_3$ salt. This suggests that Tb forms chemical bonds with the negatively charged phosphate group of the DNA, further corroborating our optical data on the complex formation and confirms that the nano-complexes can exist not only in solution but also in a condensed phase.

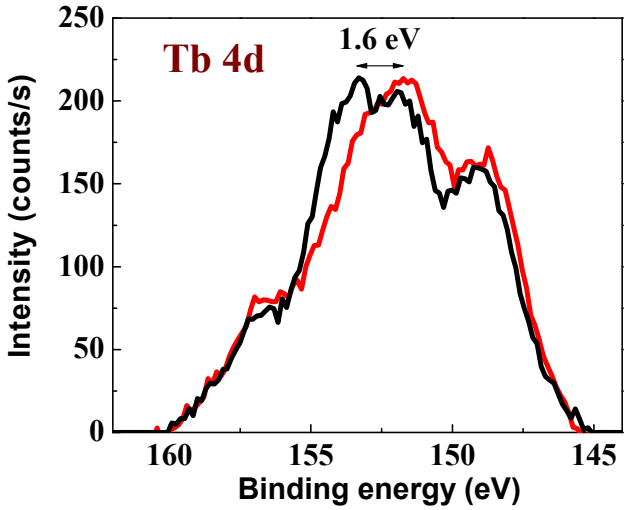

Figure 2.11: X-ray Photoelectron Spectroscopy: Tb 4d line is shown for $TbCl_3$ sample (black) and Tb/DNA/SWNT complexes (red).

Chapter 3

Micelle formation in DOC/SWNT hydrogel-encapsulated terbium: Waterproof photoluminescent complexes

In this chapter formation and evolution of highly photoluminescent complexes of rare-earth ions (REI) and bile salt molecules are discussed. Rare Earth ions are widely used as bio-labels and dyes due to their unique photoluminescence (PL) properties [65–67]. When attached to a biomolecule these ions typically exist in the partially hydrated state, with the fully hydrated state being observed for free ions in salt solution [68, 69]. PL properties of both free REIs and ions bound to single wall carbon nanotubes (SWNT) have been studied previously in water bulk solution [70] and described in the previous Chapter. The behavior of a rare earth ion in a crowded environment, inside a nanoscale water compartment or in a multicomponent solution, like an intra-cellular environment, is of significant interest.

Monitoring modification of terbium PL lifetime and its diffusion and spectral properties in a complex environment allowed us to determine the influence of nanoscale constriction and/or surfactant molecules on the REIs and to propose models for their

solvation. The surfactant we use, sodium deoxycholate (DOC), is a bile salt, which possesses exclusive biological properties. It is known to form small aggregates in water (bile salt micelles), different from typical micelles formed by other surfactants. DOC micelles are smaller, have higher surface charge density and different structure. At certain concentration and/or pH many bile salts, including DOC, form larger anisotropic complexes and then undergo liquid crystal or gel phase transformation. Bile salts readily form mixed micelles with both organic and inorganic substances, insoluble by themselves. For example, DOC is commonly used to dissolve nanotubes, separate SWNT fractions and prevent reaggregation in water solution [71, 72]. Lanthanide ions were shown to form complexes with bile salts [73, 74] and other surfactants [75].

As a prototype of a crowded environment we chose silica hydrogels. These hydrogels have pores with multiple scales, from nm to μm, and can be intercalated by various materials during the gelation stage or after synthesis. In this work samples ranging from the silica hydrogels with SWNTs dispersed with DOC, to the hydrogels with DOC, to the silica hydrogels only, as well as the bulk DOC water solutions were studied.

As shown below Tb forms a series of complexes with DOC, which revealed itself in the steady-state and time-resolved PL spectroscopy measurements. Modification of these complexes in the limited volume inside the pores of the silica hydrogel has been demonstrated and the dynamics of this process has been traced in the course of diffusion of the complexes through the hydrogel.

Terbium (III) chloride (99.99% from Sigma Aldrich) was dissolved either in deionized (DI) water or D_2O in 10% w.u. concentration. All gels were made using the standard CVD technique described in detail in paper [76]. In brief, during the hydrolysis of tetramethylorthosilicate the silica was produced in the form of primary particles with size of tens of nanometers, which aggregate and form secondary particles of μm size, making the gel structure with the interparticle pores of various sizes, filled with water solution. The DOC/SWNT/Tb hydrogel samples were prepared by using two methods: terbium chloride solution as well as the DOC-dispersed SWNTs

Figure 3.1: DOC/SWNT hydrogel sample: (bottom) original sample; (top) similar sample after several days upon adding terbium chloride.

were incorporated in the hydrogel during the synthesis. Alternatively $TbCl_3$ solution was dropped into the NMR tube with (already synthesized) hydrogel with DOC-dispersed SWNTs right before the experiment. After several days both types of Tb/DOC/SWNT hydrogel samples showed similar properties, although, the PL lifetime was found to be slightly shorter (2.1 ms compared to 2.3 ms) for the latter method (a typical sample is shown in Fig.3.1).

Time-resolved PL experiments were done using a 20 ps tunable laser source (OPG/OPA, EKSPLA model PG401) with a 486nm excitation. The laser beam was focused into the center of the sample cuvette. Perpendicular to the incident beam was a pair of collection lenses, that gathered the PL signal and focused it onto the entrance slit of a photomultiplier tube detector connected to a digital oscilloscope (Lecroy, Waverunner LT 584). Two filters: 488 long pass to cut scattered incident laser beam, and band pass 540±10 nm to extract $^5D_4 \rightarrow^7 F_5$ Tb line from the total PL signal were used. The steady-state Tb emission spectra were obtained with a Horiba JobinYvon 41000 Raman spectrometer with CW Ar laser at 488 nm of excitation.

3.1 Time-resolved spectroscopy data

Efficient photoluminescence of Tb was observed in all hydrogel samples (Fig.3.2e) despite a low absorption cross section in visible and near-UV regions. This gives an early indication of changes in the Tb solvation state. Furthermore, both the shape of steady-state PL lines and the decay time measured by time resolved PL spectroscopy vary in the hydrogel as compared to the bulk water solution. In the bulk water solution Tb exists as fully hydrated ions. Time resolved spectroscopy of Tb^{3+} gives the lifetime varying more than 5 times in different surroundings (Fig.3.2). Panel (a) shows time-resolved emission decay of the $^5D_4$ state obtained after excitation at 2.55 eV (486 nm, see Appendix for PL excitation profile) for three samples: Tb in DI water solution (blue), Tb in DOC silica hydrogel (green), and Tb in DOC/SWNT silica hydrogel (red). The curves were fitted by monoexponential decay to extract the PL lifetimes. Similar data was collected for all samples and the results are summarized in Fig.3.2c and Table 3.1. We argue that the changes in the lifetime which are directly related to the PL efficiency, reflect the structure of photoluminescent complexes of REI, forming in solution and further evolving in the nano-porous environment.

Indeed, the $^5D_4 \rightarrow^7 F_5$ electronic transition at 2.27 eV (545 nm) in Tb^{3+} is a $4f \rightarrow 4f$ transition. The valence 4f electrons are well shielded from the environment by the outer core 5s and 5p electrons and minimally involved in bonding. Because of this shielding, the properties of these ions are typically retained after complex formation. Despite this fact, the luminescence of solvated REIs is weak due to significant nonradiative recombination through the O–H vibrations of the water molecules in the solvation shell. Moreover, the spectral lines of Tb PL show characteristic broadening in water solution (to be discussed later). It has been already shown that the addition of chelating agents and encapsulation of the REIs in chelate shells or in surfactant micelles leads to longer emission lifetimes and consequently to higher quantum yields [77, 78]. Our time-resolved PL data confirm that the interaction of Tb^{3+} with DOC results in fast and efficient micelle formation to give long PL decay time, 1.5 ms and longer.

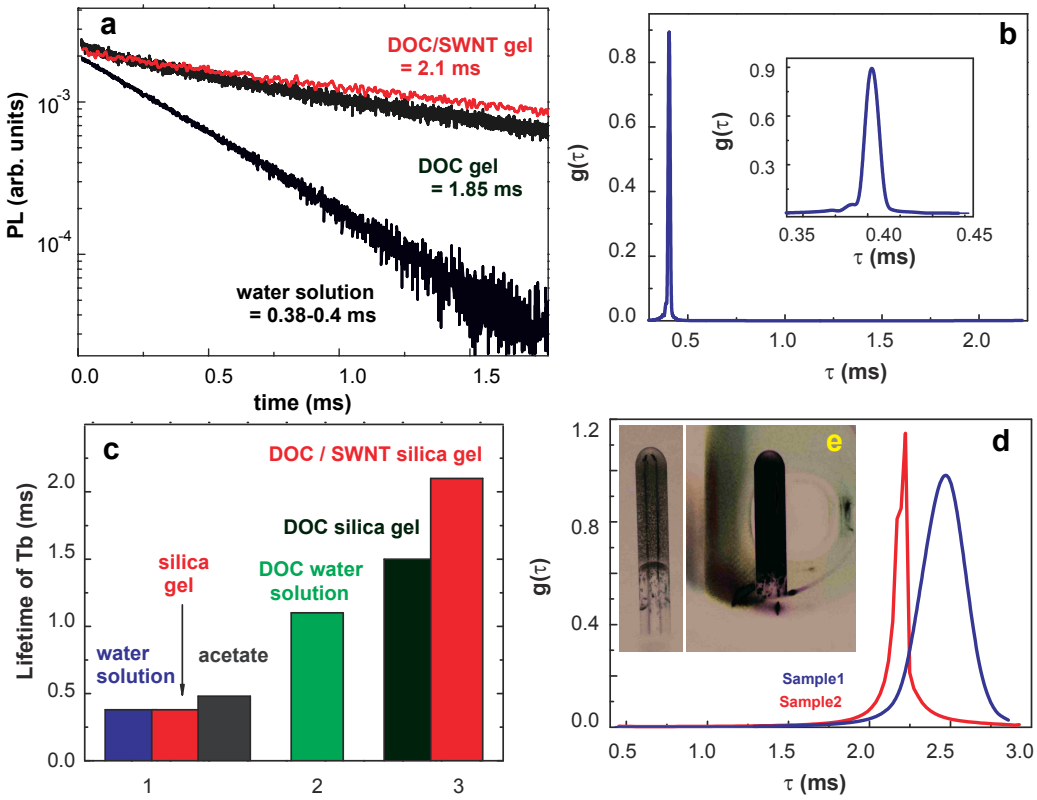

Figure 3.2: (a) Semilogarithmic plot of the PL intensity versus time ($^5D_4 \rightarrow ^7F_5$ transition in Tb at 486 nm of excitation) for solvated Tb (blue), Tb encapsulated in DOC micelles confined in the pores of DOC-hydrogel (green) and in SWNT-DOC-hydrogel (red). Spectral distribution functions for $TbCl_3$ in DI water (b) and in DOC/SWNT gel (d). (c) Correlation of the Tb lifetime with the content and morphology of Tb environment. (e) Typical Tb/DOC/SWNT hydrogel sample: image (left) and intense PL of $^5D_4 \rightarrow ^7F_5$ electronic transition at 488nm of excitation (right).

However, placing Tb^{3+} in a complex and/or crowded environment results in further improvement of the photoluminescence. Up to a 50% increase of the lifetime was observed after encapsulation in the hydrogel, following an initial increase after the micelle formation. Analysis of the values of PL lifetime suggests that our samples fall into three groups, where the Tb ion exists in different solvated/encapsulated

Table 3.1: Tb^{3+} PL lifetime of $^5D_4 \rightarrow ^7 F_5$ transition in various environment.

	Long lifetime, ms	Short lifetime, ms
DI water solution	-	0.380 ± 0.005
D2O solution	-	0.400 ± 0.005
silica hydrogel	-	0.380 ± 0.005
Tb acetate water solution	-	0.480 ± 0.005
DOC DI water solution	1.50 ± 0.02	0.40 ± 0.02
DOC silica hydrogel	1.85 ± 0.02	0.40 ± 0.02
DOC/NT silica hydrogel	2.1 - 2.3 ± 0.02	0.40 ± 0.02

states (Fig.3.2c). In the first group, which includes $TbCl_3$ water solution, Tb inside of a silica hydrogel, and terbium acetate water solution, the fully solvated (hydrated) Tb ions were found with the typical lifetime $\tau = 0.38 - 0.48ms$ (slightly higher for $Tb(CH_3CO_2)_3$ or in heavy water). The second group contains Tb ions screened from the water molecules inside the DOC micelles, suspended in solution, with the characteristic lifetime increased to $\tau = 1.5ms$. A significant increase of PL lifetime indicates the weaker interaction or smaller number of OH groups in the nearest vicinity of the Tb ion.

In the third group, even longer lifetime ($\tau = 1.85 - 2.5ms$) is achieved. However, the samples of this group show very slow dynamics: aging during several weeks was required to achieve an equilibrium state. The difference in the Tb lifetimes for hydrogels with and without nanotubes is reproducible and most likely is due to sample (gel) morphology differences. In order to prove that in group 3 this long-lived state corresponds to the Tb/DOC micelles packed in the pores of hydrogel, additional spectral data were taken (to be presented in Sec.3.2). One can reject the

model of interaction of pure Tb ions with the silica or SWNT (not involving DOC) because of the different Tb behavior in DOC gel and bulk DOC solution samples vs. samples without surfactant (gel and solution). We emphasize the strong correlation of both the lifetime and the peak shape of steady-state PL in the presence or absence of DOC. Additional evidence for Tb forming the DOC complexes is from the time-resolved PL of the transient diffusion state, presented next.

3.2 Formation and evolution of RE complexes

We observed the evolution of complexes during the diffusion of Tb^{3+} ions through the DOC/SWNT hydrogel. Fig.3.3a presents the linear-log plot of PL decay signal for Tb taken near the top of sample (location indicated by dark blue arrow in Fig.3.4, inset) with different delay times, 10 to 56 min, after $TbCl_3$ DI water solution was added at the top of the hydrogel. The PL signal at $t < 4$ min was not useful due to a low signal-to-noise ratio corresponding to vanishing concentration of REI, not penetrated in the sample yet. The curves show evolution of the Tb PL in the course of slow diffusion. The decay has stretched exponential form and is characterized by more than one lifetime. In order to clarify the nature of this non-mono-exponential decay we performed spectral analysis of the PL data which was fit by:

$$I(t) = \int g(\tau) e^{-t/\tau} d\tau \tag{3.1}$$

where $g(\tau)$ represents a spectral distribution function (SDF) and, as we show next, is characteristic of the sample.

Similar analysis has been performed for all other PL data: for example, on Fig.3.2b the typical SDF of Tb water solution is presented which shows very sharp ($\sim$0.01 ms, compare the inset) peak around 0.40 ms, the lifetime of fully solvated (free) Tb ion. Fig.3.2d shows two typical SDF spectra of Tb in DOC/SWNT hydrogel samples, with the single lifetime longer than 2 ms, although broader in Sample 1 due to experimental time resolution. This SDF data is consistent with excellent mono-exponential fit of main panel of Fig.3.2d.

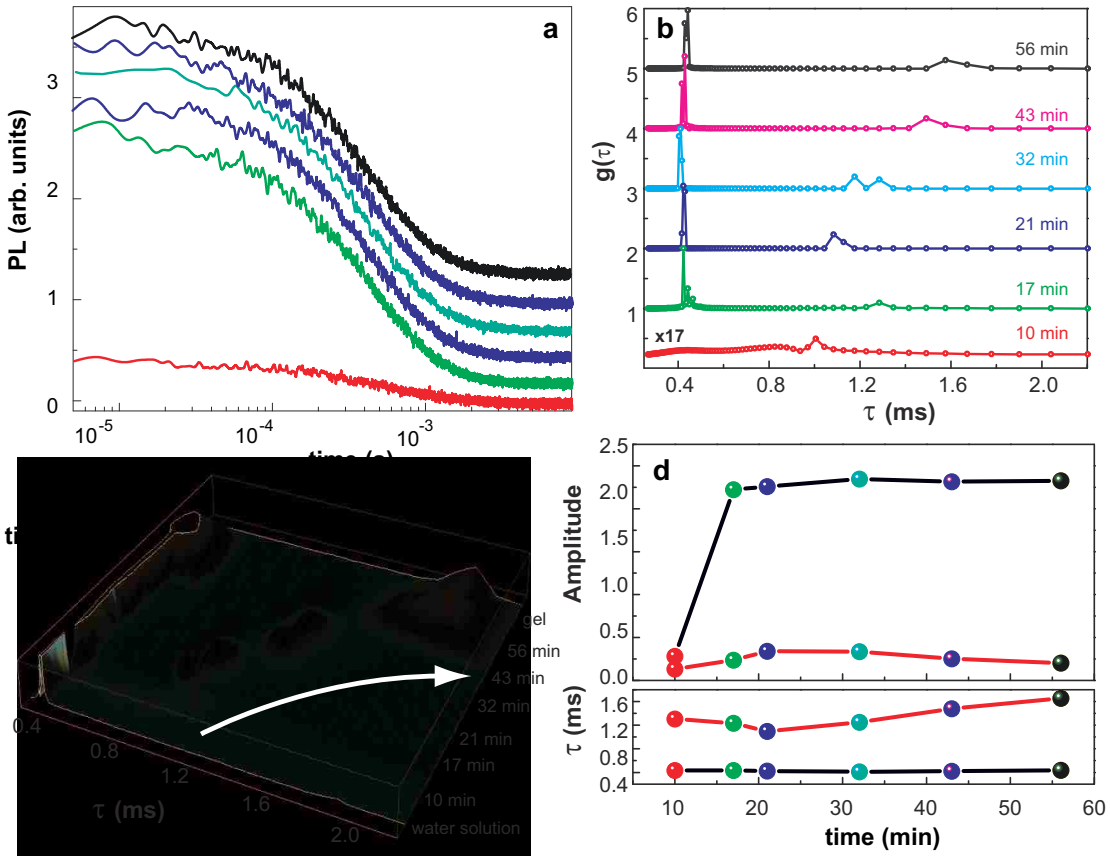

Figure 3.3: Formation and evolution of Tb-complexes upon diffusion into silica hydrogel: (a) Linear-log plot of the time-dependent PL of ${}^5D_4 \rightarrow {}^7F_5$ transition in Tb at 488 nm of excitation (the curves are offset for clarity): color code is the same as in (b) and (d). Stretched-exponential shape is consistent with two lifetimes, τ_1 and τ_2. (b) Evolution of the spectral distribution function (SDF) during the time of experiment. (c) Comparison of SDF, peaked at corresponding lifetimes τ_1 (~ 0.4 ms) and τ_2 (> 1 ms), and SDF of Tb in DI water (at the bottom of plot) and in DOC/SWNT gel (at the top, taken one week later). (d) Lifetime and amplitude of the short- (blue) and long-lived (red) states of Tb for bi-exponential fit as a function of diffusion time.

In contrast, SDF plots of Tb PL during the early stages of diffusion, presented in Fig.3.3b show clear bi-exponential distribution (except for red curve at t = 10 min where the signal is still too weak due to small amount of diffused Tb). The long-lived complex formed by the REI immediately upon diffusion in the crowded environment

of the silica hydrogel has the lifetime $\tau_2 = 1 - 1.5ms$ which is consistent with the lifetime observed in the bulk DOC solution. Increasing value of τ_2 gives us evidence that Tb ions form highly photoluminescent complexes while diffusing through the hydrogel. We argue this is due to suppression of the nonradiative recombination channel into the water vibration modes. REIs in these states are better screened from water molecules, although not as well as in the "aged" samples (Fig.3.2c). We suggest that REIs form bonds with bile salt molecules and trigger their gelation in DOC water solution and/or while diffusing through the gel matrix which contains DOC. This process is clearly seen by the color of the sample changing upon adding Tb: the samples become "milky" due to stronger light scattering by large size DOC micelles/complexes (Fig.3.1,3.2e).

Short lifetime, $\tau_2 \sim 0.45ms$, is close to the lifetime of $TbCl_3$ DI water solution (Fig.3.2a,b). Corresponding short-lived state shows a little variation during diffusion process, while the long-lived state has gradually increasing lifetime, becoming more and more stable against non-radiative recombination by water. This is further evident when all SDF data is compared with Tb in pure water and in "aged" hydrogel samples, shown in 3D plot in Fig.3.3c. An arrow indicates evolution of the long-lived Tb state, born on the early stage of diffusion into DOC inside the hydrogel, moving into the complete bile salt micelles. We emphasize that, although the short-lived state is still present at $t = 56$ min delay, it totally disappears after the long period of aging of the sample (Fig.3.2a, d). We speculate that the long-lived state corresponds to the Tb coordinated between DOC molecules, making a DOC-gel structure, still interpenetrated by water molecules. The short-lived state, with lifetime just slightly longer than in pure water solution, corresponds to Tb slowly diffusing inside the DOC-gel matrix. With time, the long-lived state forms bigger DOC micelles where Tb is fully screened from water, most likely by agglomerating several Tb ions inside a single micelle and expelling the water molecules outside. This scenario is further confirmed by analysis of the concentration of Tb in different states, presented next.

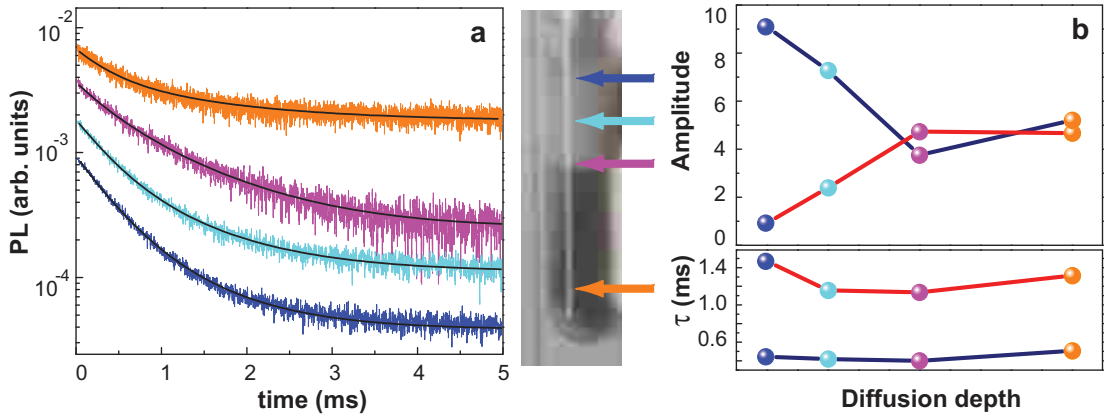

Figure 3.4: Evolution of Tb-complexes upon diffusion into silica hydrogel taken 80 min after adding Tb on the top of the sample at 4 loci: (blue-cyan-pink-brown) top-to-bottom of the sample (shown as inset): (a) Semilogarithmic plot of the PL intensity versus time (same PL line as in Fig.3.2a, the curves are offset for clarity). Solid lines show bi-exponential fit with short- and long-lifetime, τ_1 (blue) and τ_2 (red); (b) corresponding lifetimes τ_1 and τ_2, and amplitudes A_1 and A_2 for the states of Tb ions as a function of diffusion depth.

We fit the PL data in Fig.3.3a by bi-exponential decay:

$$I(t) = y_0 + A_1 exp(-\frac{t}{\tau_1}) + A_2 exp(-\frac{t}{\tau_2}) \tag{3.2}$$

where the background level, y_0, is set by the zero level of the PL signal. Resulting amplitudes (A_1 and A_2) and lifetimes (τ_1 and τ_2) are plotted vs. diffusion time in Fig.3.3d. The concentration of the short-lived state (blue) first increases abruptly, then steadily grows which corresponds to continuing diffusion of Tb inside the sample. Although the long-lived state (red) forms immediately upon diffusion, it also increases with time, due to modification of the Tb complexes. In the long run all REIs will create the long-lived complexes with DOC, given that the REI amount is not in excess.

After 80 min of diffusion we measured the spatial distribution of Tb in its complexed states ($\tau_2 > 1$ ms) and in the states accessed by water ($\tau_1 < 0.5$ ms). The results are presented in Fig.3.4 with the color code (blue-cyan-pink-brown) showing the depth of observation location (top-to-bottom). The SDF becomes broader

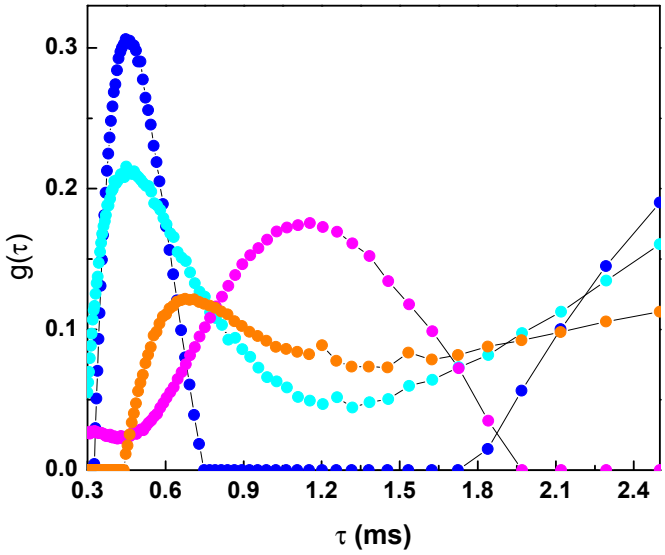

Figure 3.5: Spectral distribution function calculated for Tb-complexes upon diffusion into silica hydrogel taken 80 min after adding Tb on the top of the sample at 4 loci as in Fig.3.4

with the depth (shown in Fig.3.5) and it further shifts toward long lifetime, same as in complete DOC micelles. A bi-exponential fit gives the relative concentration of hydrated Tb and Tb complexes as a function of the diffusion depth (Fig. 3.4b). Significant amount of Tb ions exists in the long-lived, "water-resistant" complexes. Formation of such complexes happens faster than the diffusion of the hydrated ions (∼1-2 mm in 60 min). In fact, it already happened deep inside the sample at the smallest (10 min) delay, as confirmed by Fig3.3. Obviously the REIs cannot reach the bottom of the sample by mere diffusion during the delay time of the experiment. Even though, both types are present everywhere inside the sample, as shown on the top panel of Fig.3.4b. We stress that the relative abundance of hydrated ions is considerably smaller to the bottom of the tube. The A_1/A_2 ratio still decreased after the end of experiment. One should observe only "water-proof" photoluminescent complexes that involve long-lived REI in the densely packed DOC micelles after the

Table 3.2: Raman shifts observed in water and heavy water [1].

in H_2O, cm^{-1}	in D_2O, cm^{-1}
60	60
175	176
3260	2373
3426	2539
3610	2670

sample reaches equilibrium (compare Fig.3.2d). We would like to note that at the deepest sample location (orange arrow) after 80 min the Tb/DOC/SWNT system has not reached an equilibrium yet. We found that in most of our samples the diffusion is slowed down, as it should be in a crowded environment.

3.3 Steady-state spectroscopy data

Next, we present the analysis of the steady-state spectra of Tb to prove that the water is indeed eliminated in these long-lived complexes.

The steady-state PL spectroscopy measurements demonstrate the expected increase of the emission signal (Fig.3.6a) in Tb/DOC solution and even more in Tb/DOC/SWNT hydrogel. The PL Quantum Yield (QY), proportional to the non-radiative lifetime:

$$QY = \frac{\tau_{nrad}}{\tau_{rad} + \tau_{nrad}} \cong \frac{\tau_{nrad}}{\tau_{rad}} \tag{3.3}$$

increases from 1.3% in the Tb water solution to 6.4% in Tb/DOC/SWNT hydrogel and 4.9% in Tb/DOC bulk solution. Furthermore, we observed substantial changes in the peak shapes. In Fig.3.6a the PL in both DOC solution (green curve) and DOC/SWNT hydrogel (red) differ drastically from the salt solution (blue) containing

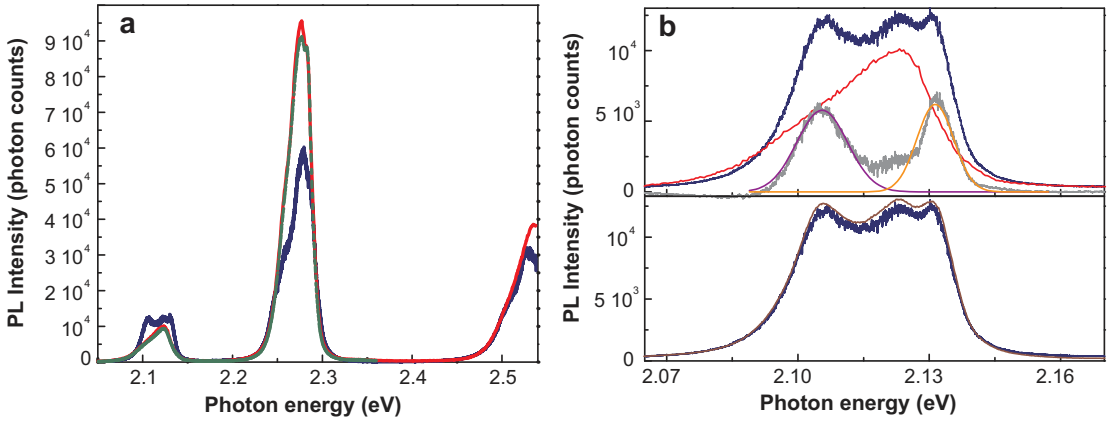

Figure 3.6: (a) PL spectra of Tb in DOC/SWNT hydrogel (red), water solution (blue), DOC water solution (green). PL of ${}^5D_4 \rightarrow {}^7F_5$ and ${}^5D_4 \rightarrow {}^7F_4$ transitions under 488 nm of excitation is measured. (b) Line shape of ${}^5D_4 \rightarrow {}^7F_4$ peak in water (blue), DOC/SWNT hydrogel (red) and their difference (black), fitted with 2 Gaussian peaks. (c) Absence of isotope shift in PL spectra of solvated Tb ion in H_2O solution (blue), D_2O solution (brown).

no surfactant. One should deliberately attribute less structured shape of these peaks to the weaker interaction with the water environment when the Tb is inside the micelles. We study the peak structure of the ${}^5D_4 \rightarrow {}^7F_4$ transition line in detail.

Fig.3.6b shows this transition for the free (solvated) Tb ion (blue) and for Tb inside the DOC micelles confined in the pores of the hydrogel (red) in detail. The curve difference (grey) fits well by two Gaussian peaks. These peaks have energies compatible with several Raman lines of O-H vibrations [1] (note that these can slightly shift in hydration water shell). We performed additional PL experiments in $TbCl_3$ solution in D_2O. No isotope effect, due to the mass difference of hydrogen and deuterium, was observed (Fig.3.6b bottom). This allows us to rule out the high frequency O-H/O-D vibrational modes that should have an appreciable isotope shift as the origin of the line shape. At the same time, the low-frequency vibrational modes of water molecules have no isotope shift [1, 79] and cannot be excluded. This line shape needs further investigation. Close similarity of the spectra of Tb in DOC micelles (in bulk light/heavy water) and inside the hydrogel confirms that the DOC gelation and following Tb encapsulation in the DOC micelles are intermediate steps

for formation of the complexes with long radiation lifetimes.

3.4 Appendix

Photoexcitation spectrum of the Tb ion

PLE of terbium is asymmetric, showing a narrow peak with a maximum at 488nm shifted toward the shorter wavelength and a line width of 4 nm. This allowed us to apply the laser line at $\lambda = 486$ nm for excitation and use the 488 nm long pass filter to cut off the scattered and/or incident laser beam.

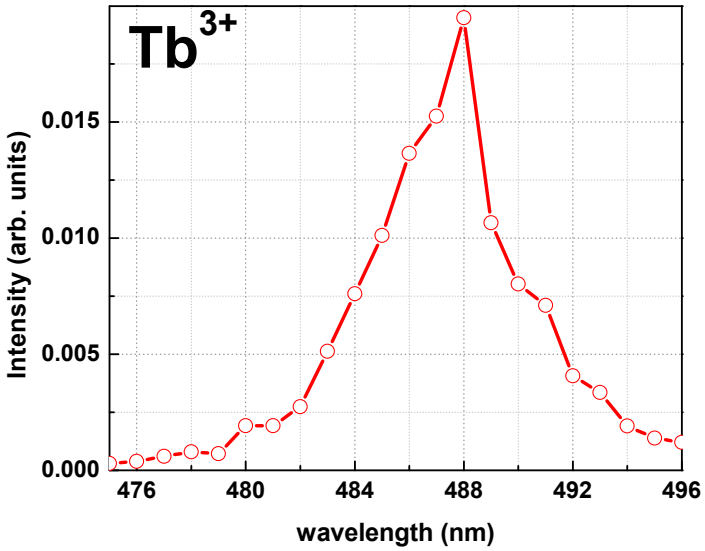

Figure 3.7: PL intensity for the peak at 545 nm vs. excitation wavelength in $TbCl_3$ DI water solution.

PL lifetime calculations

The PL of Tb/DOC solution showed the bi-exponential decay (see Eq.3.2. The short lifetime, $\tau_1 = 0.38ms$, is the lifetime of Tb ion in the solvation shell, the long-lived state, $\tau_2 = 1.5ms$, is the lifetime of Tb encapsulated in DOC micelles.

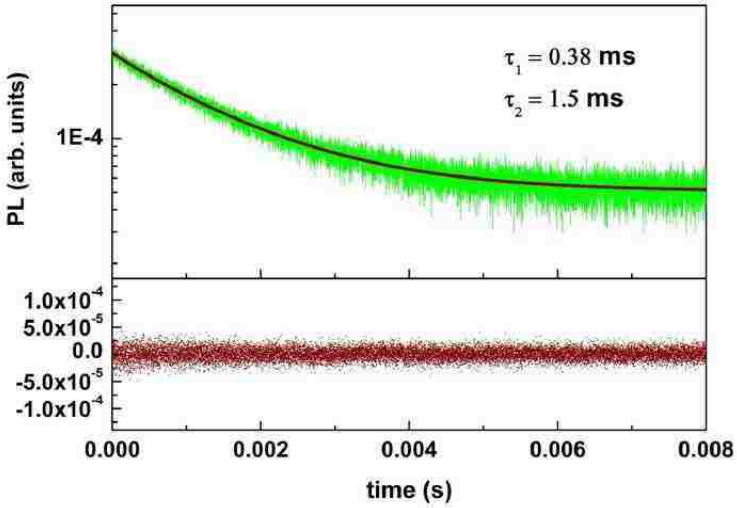

Figure 3.8: PL decay curve of Tb/DOC water solution with bi-exponential fit (overlaid) and residuals.

Each PL decay curve in Fig.3.3a was fitted by bi-exponential function(see Eq.3.2). Results are presented in Fig.3.9. We did not hold any parameter fixed (amplitude/ lifetime) during the fitting procedure. Obtained amplitudes (A_1 and A_2) and lifetimes (τ_1 and τ_2) are plotted vs. diffusion time in Fig.3.3d.

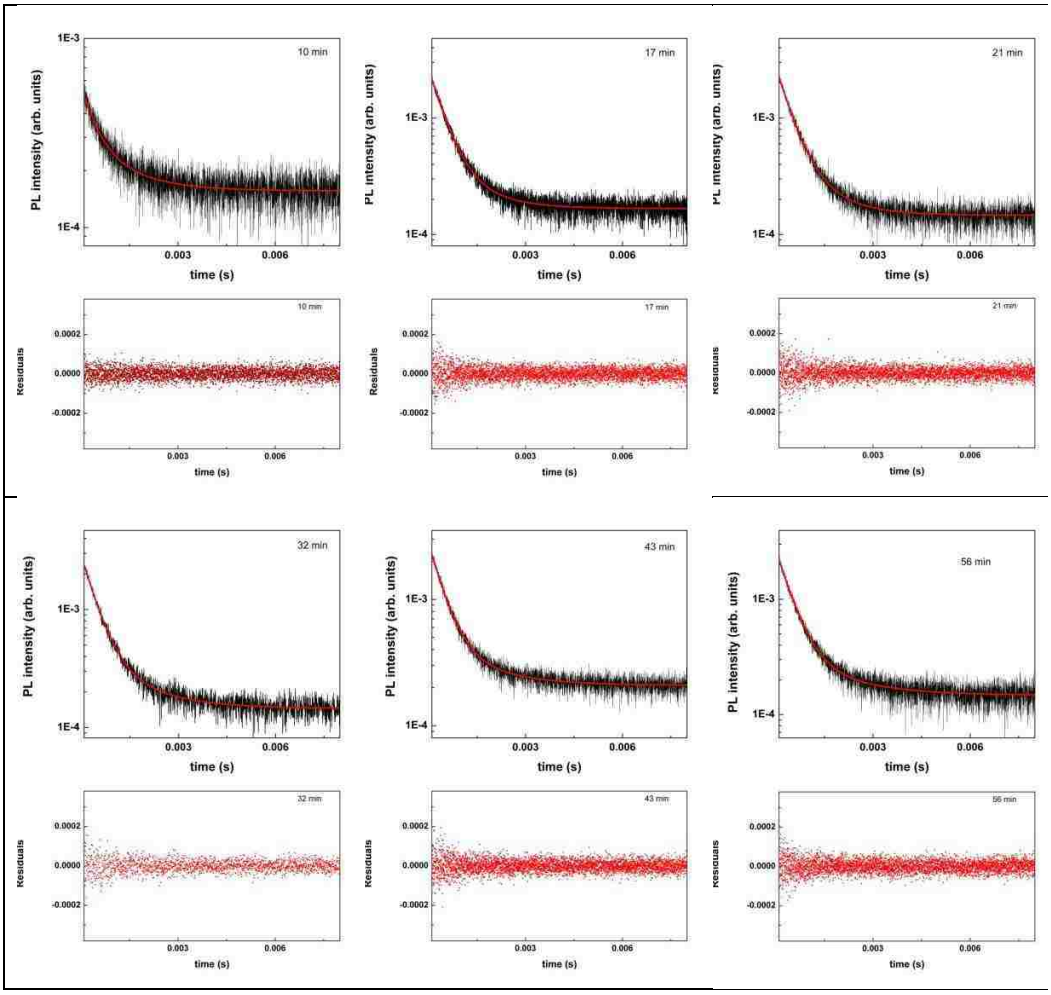

Figure 3.9: The PL decay of Tb^{3+} in DOC/SWNT hydrogel with time. Excitation wavelength is 486 nm, emission wavelength is 545 nm. Top panels show bi-exponential fit, bottom panels show residuals.

Chapter 4

Photoinduced nonradiative exciton recombination in DNA-SWNT complexes: The role of π-π^* transitions

It is well known that the optical (electronic) properties of SWNTs can be modified by functionalization. Chemical functionalization of SWNT can be achieved by either non-covalent or covalent interactions. As opposed to covalent functionalization methods, that may disrupt the sp^2-networks on the SWNT surface, non-covalent functionalization preserves most of the SWNT electronic properties. The non-covalent functionalization of SWNT has been performed with the help of various surfactants [71], porphirins [80], polyaromatic hydrocarbons [81], and polymers. The main cause for the non-covalent interaction between the SWNT and all these molecules are van der Waals and π-π stacking forces. Among a variety of polymers which have been used to make SWNT complexes, the single stranded deoxyribonucleic acid (ssDNA) is one of the most useful due to its selectivity in dispersing SWNTs of different chirality. Detailed study of DNA isolation of individual tubes, making them water soluble, and separation according to SWNT symmetry can be

found in [27]. A number of works considered effect of DNA wrapping on the optical and electronic properties of SWNTs. Still little is known about photoinduced modulation in DNA/SWNT system. Existence of photoinduced charge transfer in other DNA systems was recently demonstrated [82]. Here we apply multi-wavelength excitation spectroscopy to study the interaction of SWNT with the DNA, excited by UV light. In our two-color excitation scheme, by combining a standard visible excitation with an additional UV pump, $G_{vis} + G_{UV}$, which can be tuned to the resonant excitation of ssDNA, we observed unexpected quenching of SWNT PL for all SWNT species presented in solution (Fig.4.2). Such an effect is best explained in terms of an additional non-radiative recombination channel, created by the photo-ionized DNA.

4.1 The NIR-PL in SWNT/DNA complexes under UV illumination

The samples were prepared using the procedure described in detail before: CoMoCat SWNT were wrapped with $(GT)_{20}$ ssDNA, citric buffer was substituted from solution and sample was re-suspended in heavy water (D_2O) to remove the trace of the original buffer and free DNA. An absorption Spectrum (Fig.4.1) shows clear E_{11}, E_{22}, E_{33}, E_{44} transitions for a number of identifiable individual SWNT species. The pure DNA absorption peak (π-π^*), centered around 265 nm (4.675 eV) [2], is superimposed in the inset.

A 2D photoluminescence/photoluminescence excitation (PL/PLE) plot for the DNA/SWNT solution was taken by FLUROLOG3 over a wide range of excitation: from 250 nm to 750 nm. It shows the Stokes shift of the E_{11} transition of about 5 nm with respect to absorption peaks, typical for solutions of DNA wrapped SWNT. All experiments were performed in air at room temperature; excitation intensity was kept in the linear regime.

The second harmonic of the diffraction grating turned to the appropriate grazing angle was used for the second-color (UV) excitation, thus the wavelength of UV

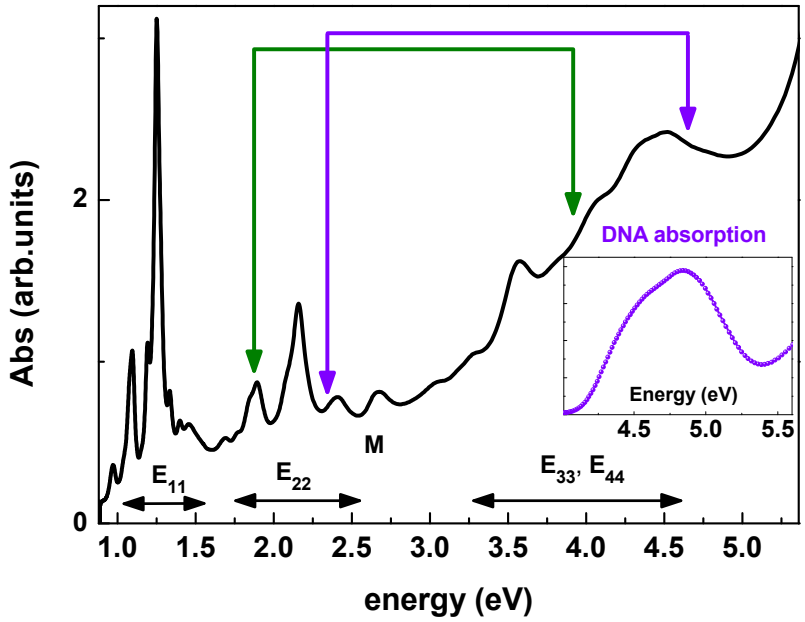

Figure 4.1: Absorption spectrum of SWNT/DNA solution. The exciton resonances are labelled. Inset shows the calculated absorption spectrum of $(GT)_{20}$ ssDNA [2].

source was always half of the one of the main excitation $\lambda_{uv} = \lambda_{vis}/2$, with the intensity approximately 10% of the intensity of the first order (in visible range) or slightly less. The ultraviolet long pass filter (UVLP, ThorLabs FEL0450) was used on the excitation pass to completely block the UV source in the reference experiments. The measured transmission spectral response of the UVLP was found to be different from the spectrum provided by the manufacturer, see Fig.4.7. Thus our own data were used to correct the excitation intensity.

The evolution of the SWNT PL upon adding a small UV pump is shown in Fig.4.2 at four different wavelengths of excitation. One can observe three different types of PL behavior.

Naturally, an additional UV illumination causes (i) a higher PL intensity in

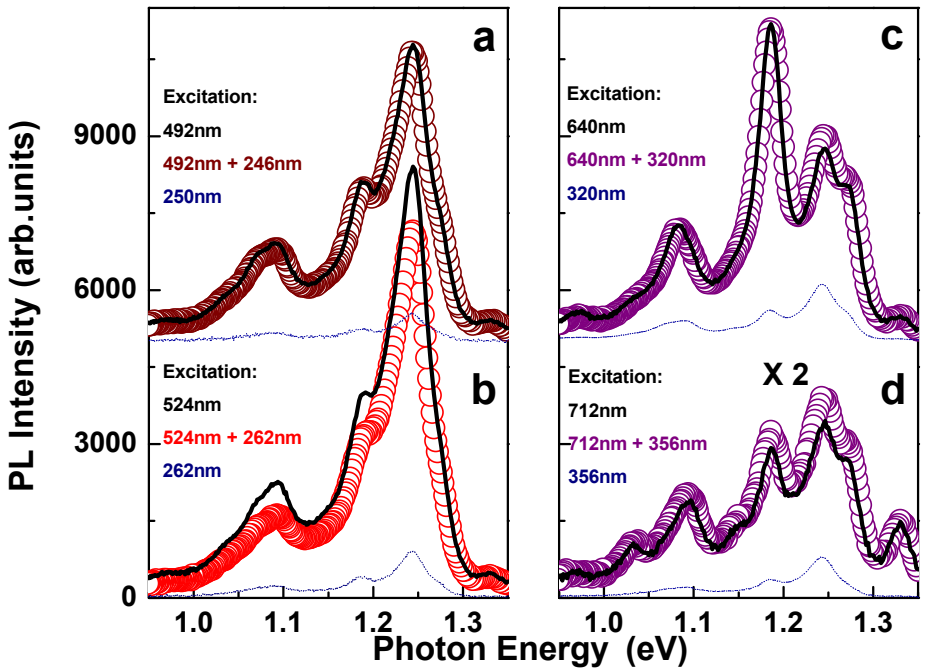

Figure 4.2: PL spectra of SWNT/DNA solution with and without an additional UV pump: emission induced by visible excitation (thick line), pure UV (thin line), and combination visible excitation and additional UV pump (symbols).

Fig.4.2c-d, as one expects, due to generation of charge carriers in the higher E_{33} and E_{44} subbands. Then these charge carriers relax from the upper subbands into the lowest subband E_{11}, form excitons and contribute to the NIR PL via their radiative recombination. Certainly, only a fraction of generated electron-hole pairs contributed to PL, the rest annihilate non-radiatively.

In Fig.4.2a (*ii*) the PL intensity has nearly the same value with and without second color excitation because none of these $E_{33/44}$ SWNT transitions are in resonance with the UV pump.

Thick black solid curves in Fig.4.2 show SWNT emission spectra taken with

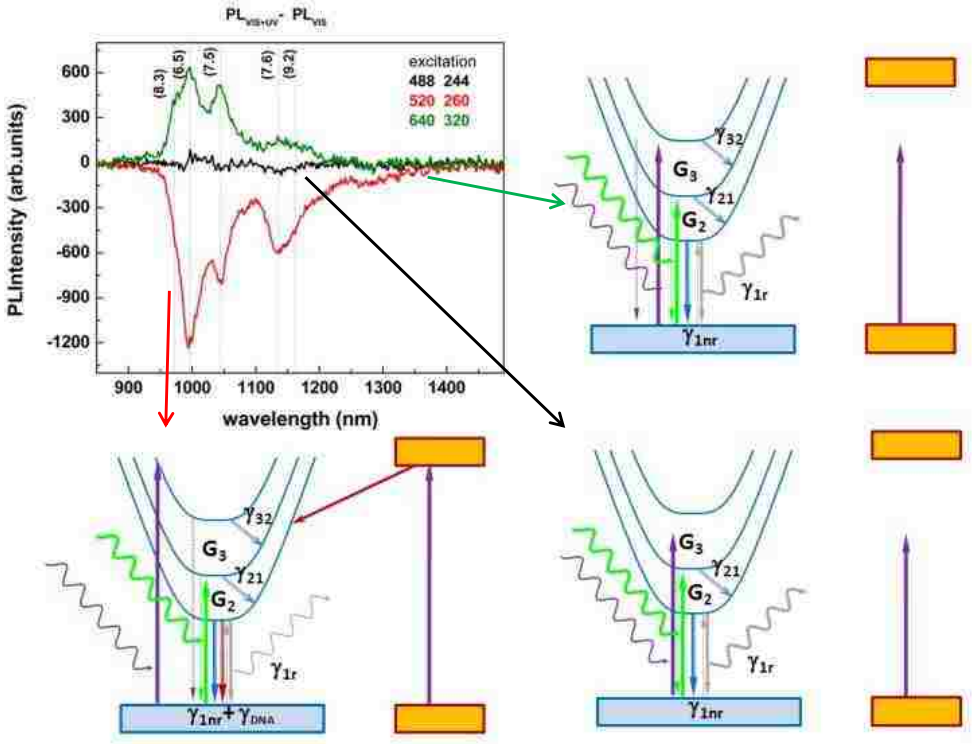

Figure 4.3: (a) PL difference; (b, c,d) schematic representation SWNT/DNA band structure.

the photoexcitation only in visible, at λ_{vis} (UV was completely filtered). The (purple/red/brown) symbols correspond to the PL with the dual-color excitation (by both visible and UV source), $\lambda_{\text{uv}} + \lambda_{\text{vis}}$. Thin curves, shown at the bottom of each plot, are given for reference and correspond to the SWNT emission observed for pure UV single-color excitation, λ_{uv}, scaled to take into account lower efficiency of the second-color excitation. It is important to note that in the first two cases (*i*-*ii*) the dual-color-excitation PL (purple and brown symbols) can be found as a simple sum of two PL spectral curves: visible excitation spectra (thick black lines, without UV pump) and UV excitation (thin, without vis pump).

The dual-color-excitation PL behavior was though drastically different in a narrow band of excitation wavelength $\lambda_{\text{vis}} = 520 \div 550$ nm. In this spectral band (*iii*)

the SWNT emission intensity shows an anomalous drop under an additional UV illumination (compare red and black curves in the Fig.4.2b). In order to provide further insight into this data we plot PL intensity difference with and without additional UV pumping in Fig.4.3.

The band structure of the SWNT/DNA hybrid is shown schematically in the side panels of Fig.4.3 for each case. We consider that resonant excitation $G_{\rm vis} = G_2$ creates an exciton in the E_{22} manifold. The exciton undergoes quick relaxation to the first subband followed by radiative recombination with γ_{r1} rate, giving rise to PL. The same exciton can annihilate via nonradiative recombination with the γ_{nr1} rate standing for total decay channel. Under $G_{\rm vis/uv}$ pump at 492/244 nm, the SWNTs cannot be excited resonantly either by $G_{\rm vis}$ or by $G_{\rm uv}$ line, as shown in Fig.4.3d. As a result the number of e-h pairs due to additional UV excitation is negligible and the PL difference is close to zero (compare thick black curve in Fig.4.3a and brown symbols in Fig.4.2a).

At 640/320 nm ($G_{\rm vis/uv}$ pump) the SWNT are resonantly excited both in visible and UV. The resonant UV excitation generates additional $e-h$ pairs in the E_{33} subband that can relax to E_{22} and subsequently to E_{11} subbands, also recombining radiatively from the lowest energy level and contributing to the PL. Then the PL difference (green curve in Fig.4.3a and purple symbols in Fig.4.2c-d) show a rise of the photoluminescence. At this particular wavelength of the second-color excitation (320 nm) the PL enhancement is due to (8,3), (6,5), (7,5) and (7,6) SWNTs.

The picture is drastically different for 520/260 nm excitation. The PL difference is negative, which means that UV illumination initiates an efficient PL quenching process. We stress that (1) PL quenching happens uniformly for all semiconducting tubes present in solution and has a similar strength for each of the PL lines. We compare the differential PL emission: $\Delta I = I^{\rm vis+uv} - I^{\rm vis}$, and one-color excitation spectrum $I^{\rm vis}$ in Fig.4.4 to verify that all features assigned to particular chiralities are present in the same proportion. Thus this mechanism is non-discriminant with respect to SWNT chirality. At the same time, (2) this quenching process varies with the photon energy of excitation: it manifests itself in a narrow PLE spectral range which is (3) not resonant with any of E_{33} or E_{44} transitions of SWNT present in

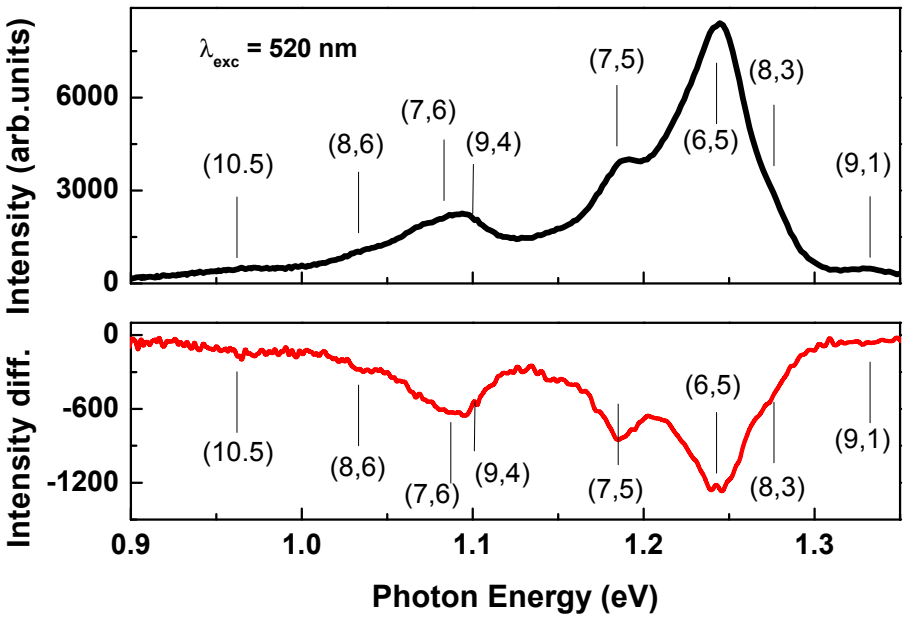

Figure 4.4: PL spectrum at 520 nm excitation(top panel) and PL difference (bottom panel) for SWNT/DNA solution.

solution 4.5.

Absence of ΔI selectivity along with the observation of a distinct PLE band and its coincidence with the spectral absorption band of the DNA at 260 nm allows us to propose that an additional nonradiative decay channel appears due to resonantly excited DNA. We note that the effect was not observed in similar SWNT samples dissolved using different surfactants, DOC/SDS, while replacement of D_2O with H_2O preserves the effect, which allows us to attribute its sole origin to DNA.

According to Fig.4.2c, the PL yield decreases under second-color UV illumination. Since $I_{PL} \propto \frac{\gamma_{r1}}{\gamma_{nr1}+\gamma_{r1}} \simeq \frac{\gamma_{r1}}{\gamma_{nr1}}$, it argues for increased non-radiative rate in the lowest exciton state. An alternative assumption – decrease of the radiative rate,– according to detailed equilibrium principle, should be accompanied with the lower

absorption (bleaching). UV irradiation was previously suggested to make direct influence on the nanotube electronic structure, for example, via UV-assisted defect creation, SWNT functionalization or formation of chemical bonds [83, 84] that lead to lower γ_{r1}. This results in typically long lasting absorption and PL bleaching effects with appreciable recovery times, while in our experiments the effect was instantaneous. Therefore we can safely exclude bleaching via UV-induced defects or SWNT chemical reactions from consideration. This is further supported by using tubes wrapped with the GT-DNA, which is known to cover the SWNT surface densely without holes, suppressing the surface functionalization [85]. Thus, we must consider that the PL yield decreases under second-color UV illumination because of an increased non-radiative rate in the lowest exciton state and exclude the lowering of γ_{r1}.

Before introducing a new nonradiative mechanism of exciton decay we briefly discuss existing ones and argue why they cannot explain our two-color PL. We outline three main groups of PL nonradiative decay channels, considered in the earlier works to be dominating under certain conditions:

1. At very high excitation intensity, when the number of excitons per SWNT is larger (much larger) than one, a multi-exciton (Auger recombination) decay mechanism [86] is important. Similar exciton-electron Auger recombination was shown to be less efficient [87, 88] than the exciton-exciton Auger channel due to strong restrictions imposed on the symmetry of electronic states participating in such a transition. These conditions are difficult to satisfy unless (non-equilibrium) charge carriers exist or unless one considers electrons in deep-band-gap, strongly localized states (see also group 3 below).

2. For excitons (or e-h pairs) in E_{22} (and higher) subband that overlap with the single-electron continuum in a lower subband (for example, E_{11}), the electron-electron [55] (or electron-phonon [89] scattering results in intersubband relaxation. This non-radiative channel naturally does not apply to E_{11} excitons, lying below the corresponding single-electron continuum of states.

3. Many-particle (multi-state) non-radiative channels can become very efficient under the assumption that (a) many-particle interaction satisfies required symmetry

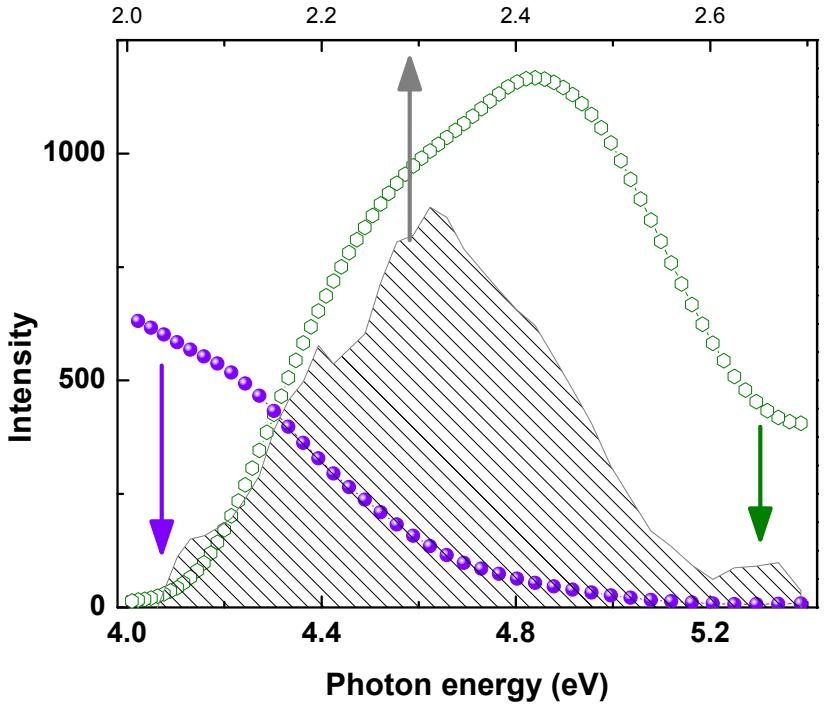

Figure 4.5: PLE spectrum for the (7,5) nanotube (purple symbols), absorption spectrum of DNA (green symbols), and normalized difference for PL with and without UV pump (gray) for SWNT/DNA solution.

selection rules and (b) the process is resonant in energy, that is, the many-particle state coincides with the energy difference between the exciton and the ground state. Such mechanisms include PAIEI [87] and a number of defect- or impurity-based exciton scattering models [41, 89–92].

Because of the perfect DNA coverage in our samples, the non-radiative exciton recombination mechanism based on additional defect formation seems unlikely. One may argue that the DNA wrapping may be corrupted during the UV irradiation. This would allow access of water molecules to the SWNT surface thus increasing the non-radiative decay. It may not happen in our samples because pure DI water was substituted for the DNA citric buffer and the solution has no free DNA during the

measurements. If the DNA would desorb from the tube walls under UV, the reverse process of restoration of the wrap will not happen for entropy reason. However, in our experiments the effect was fully reversible and recovered instantaneously after the second-color illumination was turned off. We note that we did not observe the effect in DOC or SDBS suspended tubes, where the concentration of the free surfactant in solution is always high and surfactant molecules may indeed exchange between solvated phase and the phase agglomerated on the tube surface [93, 94]. [1]

In our experiments, the excitation power was 6×10^{-5} light quanta per tube, always below the limit of creating multiple excitations per tube. Thus any exciton-exciton interaction mechanisms can be disregarded under main (visible) excitation, and even more under weaker UV illumination.

Finally, the exciton decay rate of the lowest subband is responsible for the PL yield. This excludes the intersubband relaxation mechanisms, due to non-overlap of E_{11} exciton with its continuum. Then only mechanisms involving free charge carriers need to be considered.

It is known that additional free charge carriers enhance nonradiative recombination rates [95, 96]. One should distinguish, however, direct UV generation of the e-h pairs in the upper SWNT subbands. This exciton generation shows a resonant enhancement at the PLE lines of these subbands and varies with SWNT chirality. Direct UV pump still leaves the total charge density of SWNT the same, since generation by itself does not break the charge neutrality. Thus it does not lead to a tube doping and cannot explain changes in the PL yield unless additional trapping mechanisms would be invoked.

Therefore, one has to assume that there is a new mechanism, providing a steady-state doping of the SWNT, possibly due to a resonant photoexcitation of the surrounding. The photoexcited states should be shallow enough to allow fast "instantaneous" response upon turning two-color excitation on and off. An interesting PL

[1] We cannot exclude that UV irradiation may influence the ends of the tubes which are open to water, however to the best of our knowledge such mechanism has not been observed before and it should be negligible for the length of our tubes ~ 400 nm.

behaviour coincident with the complex formation with the multivalent ions, as described in Chapter 2, was observed under UV illumination and it is worth future study.

What could be the origin of these shallow states? We speculate that the resonantly photoexcited DNA undergoes π-π^* transition, with the energy of the excitation above the forbidden gap of the DNA ~ 4.2 eV, and then transfers the excited charge carrier into the SWNT conduction bands. Similar charge transfer has been observed earlier in other SWNT hybrids: with porphyrines [80] , fullerenes [97], and organic molecules [98]. Indeed the DNA ionization potential is 8.9-9.3 eV and 8.25-8.62 eV [99, 100] for thymine and guanine bases correspondingly, it can vary in different solvation states. This allows us to estimate the position of the excited π^* state to be in the resonance with the conduction bands of a typical SWNT, which has a work function of the order of 5 eV and a half of the band gap $\sim 0.5 - 0.8$ eV.

We assume that the photoexcited DNA electron can autoionize in the SWNT conduction bands. This creates an additional free charge carrier density on the tube (although the whole complex DNA/SWNT is electrical neutral), which facilitates electron-electron scattering and non-radiative decay of E_{11} exciton. Such a mechanism would not differentiate SWNTs of different chirality unless the photoexcited state moves out of the resonant window, thus decreasing the autoionization rate. This, however, would require tubes with extremely large band gap, not found in our samples. From our data we cannot exclude any of known non-radiative mechanisms promoted by free charge carriers (PAIEI, e-e interaction, trion-exciton dissociation). Instead we analyze this decay channel phenomenologically as described next.

We propose a model to explain all experimental data. Assuming that the exciton kinetics is governed by a 3-level rate equation and making a few approximations to be listed next, we derive a simple equation relating an additional non-radiative decay rate, γ_{DNA}, to experimental data. In deriving this equation we made the following approximations, all justified in our case: (i) conversion rate for relaxation of direct UV generated excitons from E_{33} into E_{22} is considered to be a constant of the order of 1/2 or slightly larger: $QY_3 = \gamma_{32}/(\gamma_{32} + \gamma_{nr3} + \gamma_{r3}) \simeq \eta_{32} \sim O(1)$. This constant conversion rate is considered to be already included in $\eta_{\rm uv}$, the total efficiency of

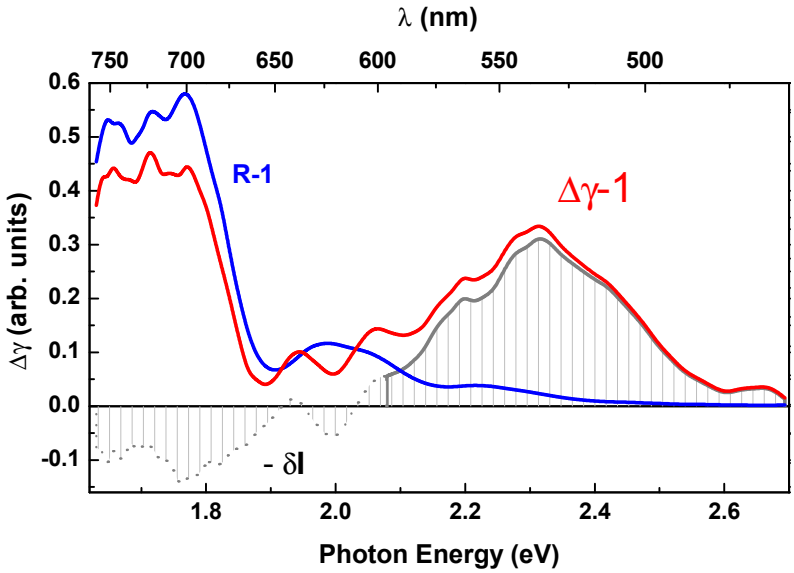

Figure 4.6: Calculated non-radiative decay rate, associated with the DNA autoionization channel (red); normalized difference for PL with and without UV pump (gray); UV pump efficiency (blue).

UV pump (see below in Eq.4.4). (ii) The effect of DNA autoionization needs to be reflected only in the E_{11} exciton subband. This is correct unless the highest $\pi - \pi^*$ transitions that can overlap with the very bottom of E_{22} subband are most important. Lastly, (iii) we neglect the radiative recombination rate $\gamma_{r1} \sim 0.1{-}1\ ns^{-1}$ compared to the nonradiative rate $\gamma_{nr1} \sim 0.1 - 0.5\ ps^{-1}$.

We provide below the derivation of the expression for an additional non-radiative decay rate, which we associate with the DNA autoionization channel:

$$\frac{\gamma_{DNA}}{\gamma_{nr1}} = \frac{\gamma_{total} - \gamma_{nr1}}{\gamma_{nr1}} \simeq \Delta_\gamma - 1 \tag{4.1}$$

here γ_{nr1} is the non-radiative recombination rate in E_{11} subband for one-color (vis)

excitation; $\gamma_{total} = \gamma_{DNA} + \gamma_{nr1}$ is a similar total non-radiative rate under two-color excitation. The function

$$\Delta_\gamma = R\,(1 - \delta I) \tag{4.2}$$

provides the spectral (PLE) dependence of the effect, where we use differential PL function (normalized difference for PL with and without UV pump)

$$\delta I = \Delta I / I^{\text{vis+uv}} = (1 - T_{UVLP}^{-1} I^{\text{vis}} / I^{\text{vis+uv}}) \tag{4.3}$$

and excitation ratio (the function giving the efficiency of the UV pump compared to main, visible pump):

$$R = 1 + \eta_{\text{uv}} G_{\text{uv}} / G_{\text{vis}}, \tag{4.4}$$

here I^{vis} and $I^{\text{vis+uv}}$ are the PL intensity under one-color (vis) and two-color (vis+uv) excitation correspondingly; T_{UVLP} is the correction transmission function of the UVLP filter (Fig.4.7); G_{uv} and G_{vis} are the experimentally measured excitation functions for one-color illumination; and η_{uv} is the UV pump efficiency $\sim 10\%$.

4.2 Rate equations and decay rate for DNA-based channel

We use rate equations for a three level system of exciton manyfolds, E_{ii} where $i = 1, 2, 3$ is the subband index, coupled to each other and to the ground state. In addition to standard coupling parameters $\gamma_{ij}, \gamma_{ri}, \gamma_{nri}$, known from previous works on monochromatic excitation, we add a new non-radiative decay rate: γ_{DNA}, specific for the nonradiative recombination channel induced in the E_{11} subband by the second-color photoexcitation (UV). We assign this channel to the photoexcitation of the

DNA followed by autoionization in the E_{11} subband:

$$\begin{aligned}
\frac{dn_1}{dt} &= -\gamma_{r1}n_1 - \gamma_{nr1}n_1 - \gamma_{DNA}n_1 + \gamma_{21}n_2 \\
\frac{dn_2}{dt} &= -\gamma_{r2}n_2 - \gamma_{nr2}n_2 - \gamma_{21}n_2 + \gamma_{32}n_3 + G_{\text{vis}} \\
\frac{dn_3}{dt} &= -\gamma_{r3}n_3 - \gamma_{nr3}n_3 - \gamma_{32}n_3 + \eta G_{\text{uv}},
\end{aligned} \tag{4.5}$$

where n_i is the exciton population of the i^{th} level (the E_{ii} state), G_{vis}, G_{uv} are generating functions (excitation spectral functions), η is the second-color excitation efficiency, γ_{ij} are intersubband relaxation rates, and γ_{ri}/γ_{nri} are the radiative/nonradiative rates of the corresponding states. Radiative and nonradiative rates were taken from [55, 61, 89] and presented in Table 4.1. Generating functions were directly measured with the single-color excitation and presented below.

Table 4.1: Rate equation parameters for SWNT/DNA PL quenching.

γ_{r1}	γ_{nr1}	γ_{r2}	$\gamma_{nr2,3}$	$\gamma_{21,32}$
$1.6ns$	$20ps$	$1ns$	$13fs$	$13fs$

In the steady-state in Eq.(4.5) left hand side equals zero, allowing simple solution for the populations of the states, n_i, if the generation spectral functions $G_{\text{vis,uv}}$ are known. In neglecting the radiative transition from all levels except for the lowest one, the total PL intensity is given by the product of the radiation rate of this level and it's population factor: $\gamma_{r1}n_1$. After simple math it can be written as the product of three terms:

$$\begin{aligned}
I^{\text{uv+vis}} = \gamma_{r1}n_i = &\left(G_{\text{vis}} + \eta G_{\text{uv}}\frac{\gamma_{32}}{\gamma_{32}+\gamma_{r3}+\gamma_{nr3}}\right) \\
&\times \left(\frac{\gamma_{21}}{\gamma_{21}+\gamma_{r2}+\gamma_{nr2}}\right)\left(\frac{\gamma_{r1}}{\gamma_{r1}+\gamma_{nr1}+\gamma_{DNA}}\right)
\end{aligned} \tag{4.6}$$

where the term $QY_3 = \gamma_{32}/(\gamma_{32}+\gamma_{r3}+\gamma_{nr3})$ accounts for the relaxation of the charge carriers from E_{33} subband into E_{22} subband, second term is a similar yield

for intersubband relaxation of E_{22} charge carriers into E_{11} subband, and the last term is PL efficiency in the lowest E_{11} subband. Here we specifically included additional non-radiative relaxation rate due to the photoexcited DNA: γ_{DNA}. We assume that the conversion rate in the upper subbands is large: $\gamma_{32}/(\gamma_{32}+\gamma_{r3}+\gamma_{nr3}) \approx 1/2$ or larger and that it is independent of the excitation energy which assumption is probably accurate due to the fast and efficient intrasubband relaxation. Then it can be included together with the UV efficiency in a single factor η_{uv}, and we rewrite the solution as:

$$\begin{aligned} I^{\mathrm{uv+vis}} = G_{\mathrm{vis}} &\left(\frac{\gamma_{21}}{\gamma_{21}+\gamma_{r2}+\gamma_{nr2}}\right)\left(\frac{\gamma_{r1}}{\gamma_{r1}+\gamma_{nr1}}\right) \\ \times &\left(1+\eta_{\mathrm{uv}}\frac{G_{\mathrm{uv}}}{G_{\mathrm{vis}}}\right) \quad \left(\frac{\gamma_{r1}+\gamma_{nr1}}{\gamma_{r1}+\gamma_{nr1}+\gamma_{DNA}}\right) \end{aligned} \tag{4.7}$$

where all terms except for the last two can be related to the PL intensity at the single-color (visible) excitation. In order to compare this with the experimental data one needs to correct the generation spectral function by the transmission through UVLP filter. We had to measure this correction function ourselves due to found inconsistency with the nominal transmission data presented by the manufacturer (see Fig.4.7). Finally, the PL intensity (while blocking UV-line by filter) can be described as:

$$I^{\mathrm{vis}} = \tilde{G}_{\mathrm{vis}}\left(\frac{\gamma_{21}}{\gamma_{21}+\gamma_{r2}+\gamma_{nr2}}\right)\left(\frac{\gamma_{r1}}{\gamma_{r1}+\gamma_{nr1}}\right) \tag{4.8}$$

where $\tilde{G}_{\mathrm{vis}} = G_{\mathrm{vis}}T_{UVLP}$ is the visible excitation spectral function corrected for UVLP filter transmission.

Two-color PL intensity is then:

$$I^{\mathrm{uv+vis}} = \frac{I^{\mathrm{vis}}}{T_{UVLP}}\left(1+\frac{\eta_{\mathrm{uv}}G_{\mathrm{uv}}}{G_{\mathrm{vis}}}\right)\left(\frac{\gamma_{r1}+\gamma_{nr1}}{\gamma_{r1}+\gamma_{nr1}+\gamma_{DNA}}\right) \tag{4.9}$$

We did not make any approximation in this expression yet, except for constant η_{uv} which includes constant QY_3. For the sake of transparency we can neglect in the further analysis the radiative rates compared to nonradiative ones, that are at least 2-3 orders of magnitude larger. It will be also useful to resolve Eq.(4.9) for γ_{DNA},

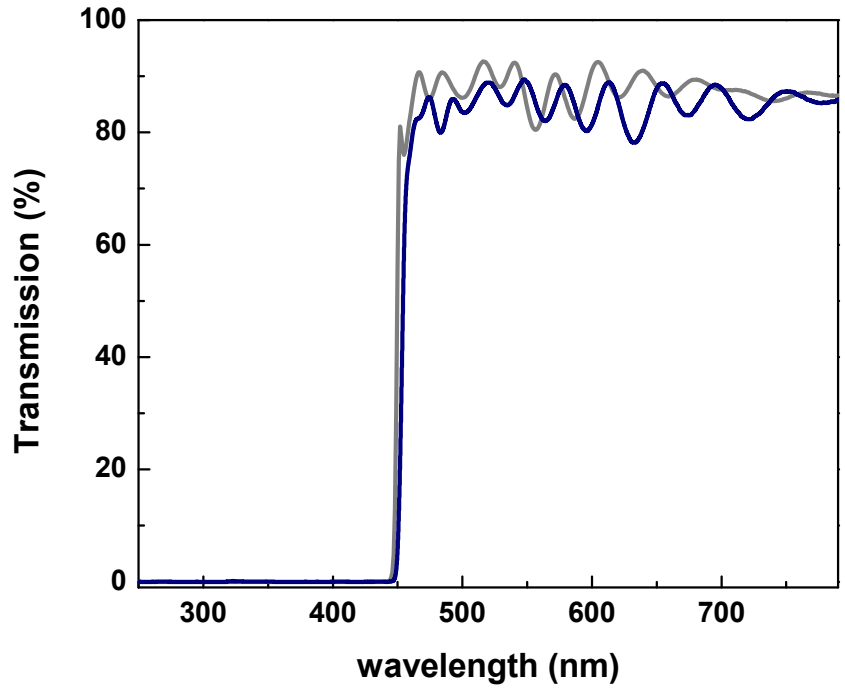

Figure 4.7: Transmission spectrum of Ultraviolet Long Pass Filter: experimentally measured (blue), from ThorLabs site (gray).

.

which solution is given by:

$$\gamma_{DNA} = (\gamma_{nr1} + \gamma_{r1}) \left(\frac{\frac{I^{\text{vis}}}{T_{UVLP}} \left(1 + \eta_{\text{uv}} \frac{G_{\text{uv}}}{G_{\text{vis}}}\right)}{I^{\text{vis+uv}}} - 1 \right) \tag{4.10}$$

where no approximation has been made yet. We remind that in here I^{vis} and $I^{\text{vis+uv}}$ are the PL intensity under one-color (vis) and two-color (vis+uv) excitation correspondingly; T_{UVLP} is the correction transmission function of the UVLP filter; G_{uv} and G_{vis} are the experimentally measured excitation functions for one-color illumination; and η_{uv} is the UV pump efficiency $\sim 10\%$. This expression shows that the anomalous spectral range of negative differential PL (when the ratio of

one-color and two-color intensities, including correction factors, is less than unity) is the indicator for the DNA-based quenching mechanism. The DNA decay rate can be obtained quantitatively from the measured data as a percent of the total decay rate in one-color scheme $\gamma_{nr1} + \gamma_{r1}$, which is well known from recent works.

It is useful to combine terms in Eq.(4.10) which are responsible for different physics of two-color PL. First we single out the corrected excitation ratio: $R = 1+\eta_{\rm uv}G_{\rm uv}/G_{\rm vis}$ which simply shows how efficient is the second-color pump compared to the main color source. Total excitation is given by:

$$G_{\rm total} = G_{\rm vis}\ R = G_{\rm vis} + \eta_{\rm uv}G_{\rm uv}. \tag{4.11}$$

When $R > 1$ the UV excitation creates non-negligible number of excitons which gives rise to total PL.

We defined earlier the corrected differential PL spectrum as $\Delta I = I^{\rm vis+uv} - T_{UVLP}^{-1} I^{\rm vis}$ which is positive if (under two-color excitation) UV pump generates additional excitons giving rise to PL. Corresponding relative differential PL can be defined as the ratio:

$$\delta I = \frac{\Delta I}{I^{\rm vis+uv}} = \left(1 - \frac{T_{UVLP}^{-1} I^{\rm vis}}{I^{\rm vis+uv}}\right) \tag{4.12}$$

Finally we define the spectral function $\Delta_\gamma = R\ (1 - \delta I)$ as the product of differential PL δI and excitation ratio R.

4.3 Analysis of $\triangle_\gamma$ spectral function in the limits of low UV excitation and low DNA absorption

Next we analyze three limiting cases for Eqs.(4.9-4.10). We start with the trivial case when both UV pump efficiency $\eta_{\rm uv}$ and DNA-based nonradiative channel efficiency γ_{DNA} are close to zero. Then the difference between the PL intensity with and without UV pump (corrected for UVLP filter transmission function) should be nearly zero, linearly proportional to both efficiencies, although entering with the different sign:

$$\Delta I = I^{\rm uv+vis} - \frac{I^{\rm vis}}{T_{UVLP}} \simeq I^{\rm uv+vis}\left(\eta_{\rm uv}\frac{G_{\rm uv}}{G_{\rm vis}} - \frac{\gamma_{DNA}}{\gamma_{nr1}}\right) \tag{4.13}$$

This equation already shows us that the processes of direct UV pumping and DNA-based quenching are competing with each other. In the region of excitation where DNA absorption is absent the second term vanishes and we have positive gain in the differential PL, as shown in Fig.4.2(c-d). With increasing role of γ_{DNA} one can observe zero difference (as in Fig.4.2(a)). If the first term is negligible, then the difference is negative (anomalous differential PL in Fig.4.2(b)). In this case the spectral PLE shape of the DNA-based nonradiative decay channel can be obtained from the differential two-color PL data as follows:

$$\begin{aligned}\gamma_{DNA} = \gamma_{nr1}(\Delta_\gamma - 1) \simeq \gamma_{nr1}\left(\frac{T_{UVLP}^{-1} I^{\text{vis}}}{I^{\text{vis+uv}}} + \eta_{\text{uv}}\frac{G_{\text{uv}}}{G_{\text{vis}}} - \ldots\right) \\ = \gamma_{nr1}\left(1 - \delta I + R - 1 - \ldots\right) = \gamma_{nr1}\left(-\delta I + R - \ldots\right)\end{aligned} \tag{4.14}$$

here we again neglect γ_{r1} compared to γ_{nr1} and skip terms that are not linear in η_{uv} or γ_{DNA}. This equation shows that the effect (first term) is either masked or even compensated by the direct pump (second term).

In the limit of negligible DNA absorption $\gamma_{DNA} \ll \gamma$ the first term $(1 - \delta I)$ disppears. In this limit the differential PL is fully determined by the excitaation ratio:

$$\delta I \simeq R - 1 - O(\gamma_{DNA}). \tag{4.15}$$

The differential function then shows the same features as the PLE of the sample. Corresponding data for several SWNT chiralities are shown in Fig.4.8.

In the limit of small UV pump efficiency (for example, due to negligible non-resonant η_3 and not because of the vanishing intensity of source, G_{uv}) and significant contribution of the DNA mechanism, one obtains for the differential PL function:

$$\delta I \simeq \frac{T_{UVLP}^{-1} I^{\text{vis}}}{I^{\text{vis+uv}}}\left(-\frac{\gamma_{DNA}}{\gamma_{total} + \gamma_{DNA}} + O(\eta_3)\right) \tag{4.16}$$

Since both γ_{DNA} and $\gamma_{total} = \gamma_{nr1} + \gamma_{r1}$ are positive and so the PL intensities are, this equation has solution only if $\delta I \leq 0$ which manifests the PLE range of DNA-based nonradiative recombination. Under the same assumptions the spectral shape of the additional nonradiative rate is given by:

$$\gamma_{DNA} \simeq \gamma_{total}\frac{-\Delta I}{I^{\text{vis+uv}}} \tag{4.17}$$

which also requires $\Delta I \leq 0$ or, the same: $I^{\text{vis+uv}} \leq T_{UVLP}^{-1} I^{\text{vis}}$.

4.4 Effect of DNA wrap on the SWNT PL quenching under UV pump

Since UV modulation of the PL signal happens for all SWNT chiralities we can single out contributions of the individual species. Fig.4.6 shows the PLE spectrum with and without UV pump detected at 1.19 eV (1041 nm), corresponding to the large peak in Fig.4.3a of the (7,5) SWNT. The differential PL, $-\delta I$, for the same tube is shown in Fig.4.6 (gray line) along with the excitation function $R-1$ (blue) and $\Delta_\gamma - 1$ (red). The function $-\delta I$ shows a positive region where the UV quenching of the (7,5) SWNT PL happens. The negative region corresponds to simple UV pump. Eqs.(4.13-4.17) show that for the DNA-based nonradiative recombination the function $\delta I \leq 1$. This effect is shadowed by the strong direct UV pump if the efficiency ratio function $R \gg 0$.

This can be better understood by comparing δI to $R-1$, the UV excitation efficiency function. In our samples this function prevails over the DNA-based quenching at $\lambda_{\text{uv}} \gtrsim 650$ nm. On the other side, the UV pump of the second color source has very weak influence on the PL of the (7,5) tube. As a result, the decay rate associated with the two-color experiment should be analyzed in terms of DNA-photoionization below 650 nm, and on the opposite it is a simple addition of PL due to two pumps above this wavelength. UV intensity of the source was negligible above $\lambda_{\text{uv}} \lesssim 230$ nm, which did not allow us to probe the whole range of the DNA absorption in the deep UV.

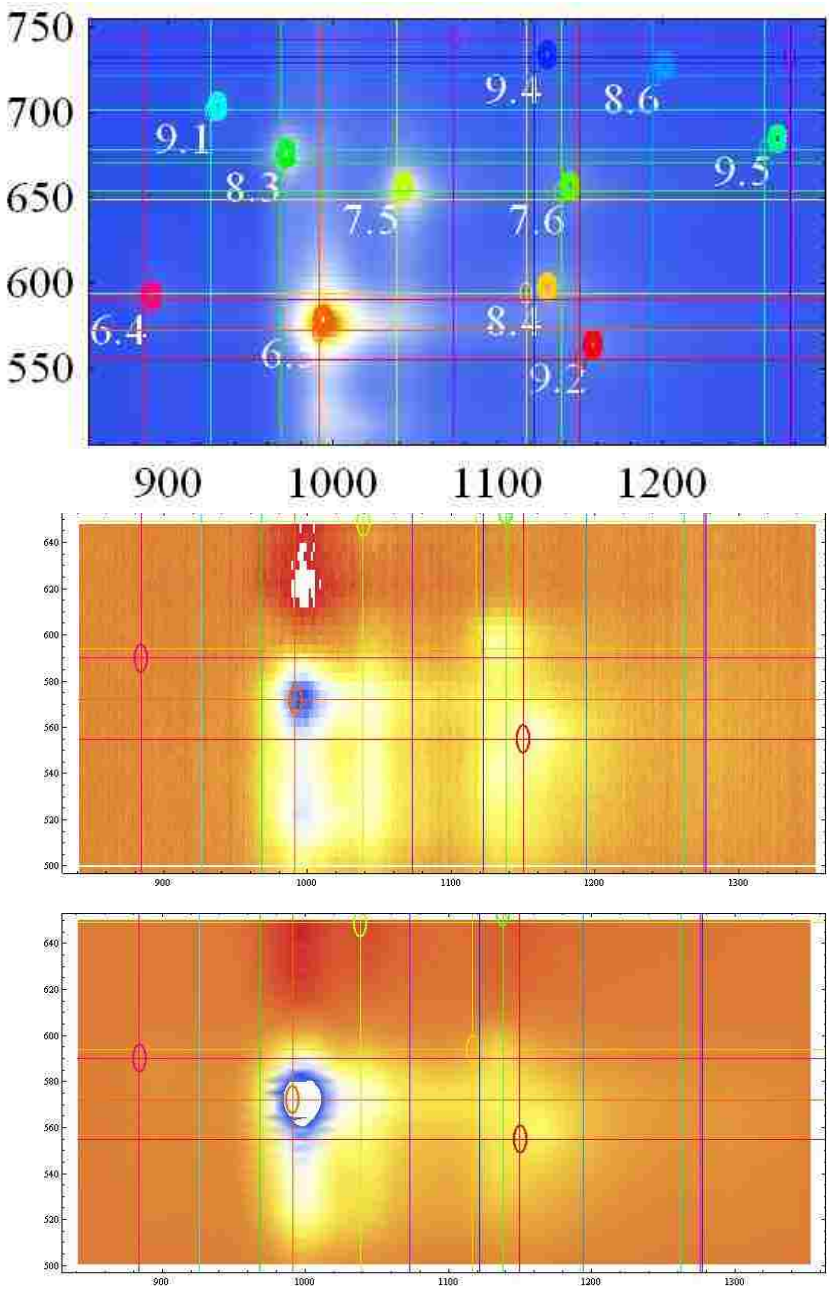

Figure 4.8: (a)PL/PLE map of SWNT/DNA solution; (b) Result of subtraction experimental PL/PLE with and without additional UV excitation; (c) calculated PLE difference.

Chapter 5

Conclusion

In this thesis I present results on the physics of SWNT – DNA – Rare Earth Ion systems. We started with energy transfer in the mixed solutions of unlike REIs (Tb and Eu) as well as in solutions of each of these ions with the DNA wrapped SWNTs. The FRET was detected by shortening of the REI lifetime with time-resolved PL as well as with directly induced PL spectroscopy. The characteristic distance between the donor and acceptor species has been derived from the measured FRET efficiency. This study revealed negative correlation (the repulsion with the longer distance) for Tb-Eu case and significant positive correlation (the attraction and the complex formation) for the REI-SWNT/DNA case. The data is in a good agreement with the theoretical estimates and allows to propose REIs and their FRET as a sensitive tool for detecting kinetics of interaction of SWNTs with ions in aqueous solutions.

Secondly, we studied behavior of Tb ions in different environments. We found that Tb ions quickly form long lifetime PL complexes in solutions containing surfactant (DOC) molecules. This process is faster than the diffusion through the DOC/SWNT silica hydrogel. The PL lifetime in these complexes increases to 2.3 ms for DOC/SWNT hydrogel with time. Similar changes of the shape of Tb lines of steady-state PL spectra in DOC bulk solution and DOC/SWNT silica gel, compared to $TbCl_3$ water solution, suggest the formation of DOC micelles in both cases. An additional increase of PL signal (and lifetime), reproducibly observed upon diffusion of Tb-DOC micelles inside the crowded environment of the hydrogel, should be due

to the nanoscale constriction inside the pores between the silica primary particles. The general increase of Tb lifetime in gels also containing SWNTs is suggestive of a special role such one-dimensional objects may play in templating surfactant structures within the silica gel. Such templating behavior in mesoscopic gels is of significant interest and will be the subject of more detailed follow-on study. We observed the evolution of the long lifetime complexes during the diffusion of REI into the DOC/SWNT hydrogel. Their lifetime is steadily increasing, moving toward the longest lifetime, assigned to complete DOC micelles. These soluble REI complexes with strong and water stable PL can be useful for biophysical imaging of REIs in cells and tissues. Understanding the dynamic behavior of REI in various surrounding is important for quantitative analysis of microscopy and spectroscopy data.

And finally, a steady-state doping of the SWNT, due to a resonant photoexcitation of the DNA was detected. The PL quenching for all SWNT species presented in solution was observed. This effect was explained in terms of an additional nonradiative recombination channel, created by the photo-ionized DNA. By solving the 3-level rate equation, both UV pump efficiency and DNA-based nonradiative channel efficiency were calculated and found to be competitive. The spectral function Δ_γ manifests the PLE range of DNA-based nonradiative recombination. The data are in good agreement with the theoretical calculations.

Bibliography

[1] Narayanaswamy, P. The Raman spectra of water, heavy water and ice. *Proceedings of the Indian Academy of Sciences - Section A* **27**, 311–315 (1948). URL http://dx.doi.org/10.1007/BF03171021.

[2] Tataurov, A., You, Y. & Owczarzy, R. Predicting ultraviolet spectrum of single stranded and double stranded deoxyribonucleic acids. *Biophysical Chemistry* **133**, 66 – 70 (2008). URL http://www.sciencedirect.com/science/article/pii/S0301462207002943.

[3] Iijima, S. & Ichihashi, T. Single-shell carbon nanotubes of 1-nm diameter. *Nature* **363**, 603–605 (1993). URL http://dx.doi.org/10.1038/363603a0.

[4] Avouris, P., Freitag, M. & Perebeinos, V. Carbon-nanotube photonics and optoelectronics. *Nat Photon* **2**, 341–350 (2008). URL http://dx.doi.org/10.1038/nphoton.2008.94.

[5] Ando, K. Highly selective synthesis of z-unsaturated esters by using new horner-emmons reagents, ethyl (diarylphosphono)acetates. *The Journal of Organic Chemistry* **62**, 1934–1939 (1997). URL http://pubs.acs.org/doi/abs/10.1021/jo970057c. http://pubs.acs.org/doi/pdf/10.1021/jo970057c.

[6] Kane, C. & Mele, E. Ratio problem in single carbon nanotube fluorescence spectroscopy. *Physical review letters* **90**, 207401 (2003).

[7] Perebeinos, V., Tersoff, J. & Avouris, P. Scaling of excitons in carbon nanotubes. *Phys. Rev. Lett.* **92**, 257402 (2004). URL http://link.aps.org/doi/10.1103/PhysRevLett.92.257402.

[8] Wang, F. *et al.* Observation of excitons in one-dimensional metallic single-walled carbon nanotubes. *Phys. Rev. Lett.* **99**, 227401 (2007). URL http://link.aps.org/doi/10.1103/PhysRevLett.99.227401.

[9] Zaric, S. *et al.* Optical signatures of the Aharonov-Bohm phase in single-walled carbon nanotubes. *Science* **304**, 1129–1131 (2004). URL http://www.sciencemag.org/content/304/5674/1129.abstract. http://www.sciencemag.org/content/304/5674/1129.full.pdf.

[10] Htoon, H., O'Connell, M. J., Doorn, S. K. & Klimov, V. I. Single carbon nanotubes probed by photoluminescence excitation spectroscopy: The role of phonon-assisted transitions. *Phys. Rev. Lett.* **94**, 127403 (2005). URL http://link.aps.org/doi/10.1103/PhysRevLett.94.127403.

[11] Walsh, A. *et al.* Scaling of exciton binding energy with external dielectric function in carbon nanotubes. *Physica E Low-Dimensional Systems and Nanostructures* **40**, 2375–2379 (2008). 0707.1888.

[12] Dresselhaus, M., Dresselhaus, G., Saito, R. & Jorio, A. Raman spectroscopy of carbon nanotubes. *Physics Reports* **409**, 47 – 99 (2005). URL http://www.sciencedirect.com/science/article/pii/S0370157304004570.

[13] Loudon, R. One-dimensional hydrogen atom. *American Journal of Physics* **27**, 649–655 (1959).

[14] Lefebvre, J. & Finnie, P. Excited excitonic states in single-walled carbon nanotubes. *Nano Letters* **8**, 1890–1895 (2008). URL http://pubs.acs.org/doi/abs/10.1021/nl080518h. PMID: 18505302, http://pubs.acs.org/doi/pdf/10.1021/nl080518h.

[15] Luer, L. *et al.* Size and mobility of excitons in (6, 5) carbon nanotubes. *Nat Phys* **5**, 54–58 (2009). URL http://dx.doi.org/10.1038/nphys1149.

[16] Koyama, T., Miyata, Y., Kishida, H., Shinohara, H. & Nakamura, A. Photophysics in single-walled carbon nanotubes with (6,4) chirality at high excitation densities: Bimolecular auger recombination and phase-space filling of excitons. *The Journal of Physical Chemistry C* **117**, 1974–1981 (2013). URL http://pubs.acs.org/doi/abs/10.1021/jp312798h. http://pubs.acs.org/doi/pdf/10.1021/jp312798h.

[17] Ando, T. Effects of valley mixing and exchange on excitons in carbon nanotubes with Aharonov–Bohm flux. *Journal of the Physical Society of Japan* **75**, 024707 (2006). URL http://jpsj.ipap.jp/link?JPSJ/75/024707/.

[18] Perebeinos, V., Tersoff, J. & Avouris, P. Radiative lifetime of excitons in carbon nanotubes. *Nano Letters* **5**, 2495–2499 (2005). URL http://pubs.acs.org/doi/abs/10.1021/nl051828s. http://pubs.acs.org/doi/pdf/10.1021/nl051828s.

[19] Guo, T., Nikolaev, P., Thess, A., Colbert, D. & Smalley, R. Catalytic growth of single-walled manotubes by laser vaporization. *Chemical Physics Letters* **243**, 49 – 54 (1995). URL http://www.sciencedirect.com/science/article/pii/000926149500825O.

[20] Bronikowski, M. J., Willis, P. A., Colbert, D. T., Smith, K. A. & Smalley, R. E. Gas-phase production of carbon single-walled nanotubes from carbon monoxide via the HiPco process: A parametric study. *Journal of Vacuum Science and Technology A* **19**, 1800–1805 (2001). URL http://scitation.aip.org/content/avs/journal/jvsta/19/4/10.1116/1.1380721.

[21] Resasco, D. *et al.* A scalable process for production of single-walled carbon nanotubes (SWNTs) by catalytic disproportionation of CO on a solid catalyst. *Journal of Nanoparticle Research* **4**, 131–136 (2002). URL http://dx.doi.org/10.1023/A1020174126542.

[22] Tan, P. H. *et al.* Photoluminescence spectroscopy of carbon nanotube bundles: Evidence for exciton energy transfer. *Phys. Rev. Lett.* **99**, 137402 (2007). URL http://link.aps.org/doi/10.1103/PhysRevLett.99.137402.

[23] Luer, L., Crochet, J., Hertel, T., Cerullo, G. & Lanzani, G. Ultrafast excitation energy transfer in small semiconducting carbon nanotube aggregates. *ACS Nano* **4**, 4265–4273 (2010). URL http://pubs.acs.org/doi/abs/10.1021/nn100674h. http://pubs.acs.org/doi/pdf/10.1021/nn100674h.

[24] O'Connell, M. J. *et al.* Band gap fluorescence from individual single-walled carbon nanotubes. *Science* **297**, 593–596 (2002). URL http://www.sciencemag.org/content/297/5581/593.abstract. http://www.sciencemag.org/content/297/5581/593.full.pdf.

[25] Bachilo, S. M. *et al.* Structure-assigned optical spectra of single-walled carbon nanotubes. *Science* **298**, 2361–2366 (2002). URL http://www.sciencemag.org/content/298/5602/2361.abstract. http://www.sciencemag.org/content/298/5602/2361.full.pdf.

[26] Islam, M. F., Rojas, E., Bergey, D. M., Johnson, A. T. & Yodh, A. G. High weight fraction surfactant solubilization of single-wall carbon nanotubes in water. *Nano Letters* **3**, 269–273 (2003). URL http://pubs.acs.org/doi/abs/10.1021/nl025924u. http://pubs.acs.org/doi/pdf/10.1021/nl025924u.

[27] Tu, X., Manohar, S., Jagota, A. & Zheng, M. DNA sequence motifs for structure-specific recognition and separation of carbon nanotubes. *Nature* **460**, 250–253 (2009). URL http://dx.doi.org/10.1038/nature08116.

[28] Zheng, M. *et al.* DNA-assisted dispersion and separation of carbon nanotubes. *Nat Mater* **2**, 338–342 (2003). URL http://dx.doi.org/10.1038/nmat877.

[29] Hasan, T. *et al.* Stabilization and debundling of single-wall carbon nanotube dispersions in N-methyl-2-pyrrolidone (NMP) by polyvinylpyrrolidone (PVP). *The Journal of Physical Chemistry C* **111**, 12594–12602 (2007). URL http://pubs.acs.org/doi/abs/10.1021/jp0723012. http://pubs.acs.org/doi/pdf/10.1021/jp0723012.

[30] Liu, J. *et al.* Controlled deposition of individual single-walled carbon nanotubes on chemically functionalized templates. *Chemical Physics Letters* **303**, 125 – 129 (1999). URL http://www.sciencedirect.com/science/article/pii/S0009261499002092.

[31] Landi, B. J., Ruf, H. J., Worman, J. J. & Raffaelle, R. P. Effects of alkyl amide solvents on the dispersion of single-wall carbon nanotubes. *The Journal of Physical Chemistry B* **108**, 17089–17095 (2004). URL http://pubs.acs.org/doi/abs/10.1021/jp047521j. http://pubs.acs.org/doi/pdf/10.1021/jp047521j.

[32] Nish, A., Hwang, J.-Y., Doig, J. & Nicholas, R. J. Highly selective dispersion of single-walled carbon nanotubes using aromatic polymers. *Nat Nano* **2**, 640–646 (2007). URL http://dx.doi.org/10.1038/nnano.2007.290.

[33] Arnold, M. S., Stupp, S. I. & Hersam, M. C. Enrichment of single-walled carbon nanotubes by diameter in density gradients. *Nano Letters* **5**, 713–718 (2005). URL http://pubs.acs.org/doi/abs/10.1021/nl050133o. http://pubs.acs.org/doi/pdf/10.1021/nl050133o.

[34] Crochet, J., Clemens, M. & Hertel, T. Quantum yield heterogeneities of aqueous single-wall carbon nanotube suspensions. *Journal of the American Chemical Society* **129**, 8058–8059 (2007). URL http://pubs.acs.org/doi/abs/10.1021/ja071553d. http://pubs.acs.org/doi/pdf/10.1021/ja071553d.

[35] Blancon, J.-C. *et al.* Direct measurement of the absolute absorption spectrum of individual semiconducting single-wall carbon nanotubes. *Nat Commun* **4**, – (2013). URL http://dx.doi.org/10.1038/ncomms3542.

[36] Berciaud, S., Cognet, L. & Lounis, B. Luminescence decay and the absorption cross section of individual single-walled carbon nanotubes. *Phys. Rev. Lett.* **101**, 077402 (2008). URL http://link.aps.org/doi/10.1103/PhysRevLett.101.077402.

[37] Miyauchi, Y., Hirori, H., Matsuda, K. & Kanemitsu, Y. Radiative lifetimes and coherence lengths of one-dimensional excitons in single-walled carbon nanotubes. *Phys. Rev. B* **80**, 081410 (2009). URL http://link.aps.org/doi/10.1103/PhysRevB.80.081410.

[38] Ju, S.-Y., Kopcha, W. P. & Papadimitrakopoulos, F. Brightly fluorescent single-walled carbon nanotubes via an oxygen-excluding surfactant organization. *Science* **323**, 1319–1323 (2009). URL http://www.sciencemag.org/content/323/5919/1319.abstract.

[39] Tsyboulski, D. A., Rocha, J.-D. R., Bachilo, S. M., Cognet, L. & Weisman, R. B. Structure-dependent fluorescence efficiencies of individual single-walled carbon nanotubes. *Nano Letters* **7**, 3080–3085 (2007). URL http://pubs.acs.org/doi/abs/10.1021/nl071561s. http://pubs.acs.org/doi/pdf/10.1021/nl071561s.

[40] Rajan, A., Strano, M. S., Heller, D. A., Hertel, T. & Schulten, K. Length-dependent optical effects in single walled carbon nanotubes. *The Journal of Physical Chemistry B* **112**, 6211–6213 (2008). URL http://pubs.acs.org/doi/abs/10.1021/jp077144l. http://pubs.acs.org/doi/pdf/10.1021/jp077144l.

[41] Harrah, D. M. & Swan, A. K. The role of length and defects on optical quantum efficiency and exciton decay dynamics in single-walled carbon nanotubes. *ACS Nano* **5**, 647–655

(2011). URL http://pubs.acs.org/doi/abs/10.1021/nn1031214. http://pubs.acs.org/doi/pdf/10.1021/nn1031214.

[42] Lefebvre, J., Fraser, J., Homma, Y. & Finnie, P. Photoluminescence from single-walled carbon nanotubes: a comparison between suspended and micelle-encapsulated nanotubes. *Applied Physics A* **78**, 1107–1110 (2004). URL http://dx.doi.org/10.1007/s00339-003-2460-6.

[43] Fantini, C. *et al.* Optical transition energies for carbon nanotubes from resonant raman spectroscopy: Environment and temperature effects. *Phys. Rev. Lett.* **93**, 147406 (2004). URL http://link.aps.org/doi/10.1103/PhysRevLett.93.147406.

[44] Uryu, S. & Ando, T. Environment effect on cross-polarized excitons in carbon nanotubes. *Phys. Rev. B* **86**, 125412 (2012). URL http://link.aps.org/doi/10.1103/PhysRevB.86.125412.

[45] Ando, T. Environment effects on excitons in semiconducting carbon nanotubes. *Journal of the Physical Society of Japan* **79**, 024706 (2010). URL http://jpsj.ipap.jp/link?JPSJ/79/024706/.

[46] Miyauchi, Y. *et al.* Dependence of exciton transition energy of single-walled carbon nanotubes on surrounding dielectric materials. *Chemical Physics Letters* **442**, 394 – 399 (2007). URL http://www.sciencedirect.com/science/article/pii/S0009261407007464.

[47] Liu, K. *et al.* An atlas of carbon nanotube optical transitions. *Nat Nano* **7**, 325–329 (2012). URL http://dx.doi.org/10.1038/nnano.2012.52.

[48] Tayo, B. O. & Rotkin, S. V. Charge impurity as a localization center for singlet excitons in single-wall nanotubes. *Phys. Rev. B* **86**, 125431 (2012). URL http://link.aps.org/doi/10.1103/PhysRevB.86.125431.

[49] Spataru, C. D. & Leonard, F. Tunable band gaps and excitons in doped semiconducting carbon nanotubes made possible by

acoustic plasmons. *Phys. Rev. Lett.* **104**, 177402 (2010). URL http://link.aps.org/doi/10.1103/PhysRevLett.104.177402.

[50] Steiner, M. *et al.* Gate-variable light absorption and emission in a semiconducting carbon nanotube. *Nano Letters* **9**, 3477–3481 (2009). URL http://pubs.acs.org/doi/abs/10.1021/nl9016804. http://pubs.acs.org/doi/pdf/10.1021/nl9016804.

[51] Dexter, D. L. A theory of sensitized luminescence in solids. *The Journal of Chemical Physics* **21**, 836–850 (1953). URL http://scitation.aip.org/content/aip/journal/jcp/21/5/10.1063/1.1699044.

[52] Forster, T. Energiewanderung und fluoreszenz. *Naturwissenschaften* **33**, 166–175 (1946).

[53] Latt, S. A., Cheung, H. T. & Blout, E. R. Energy transfer. a system with relatively fixed donor-acceptor separation. *Journal of the American Chemical Society* **87**, 995–1003 (1965). URL http://pubs.acs.org/doi/abs/10.1021/ja01083a011. http://pubs.acs.org/doi/pdf/10.1021/ja01083a011.

[54] Bunzli, J.-C. G. & Piguet, C. Taking advantage of luminescent lanthanide ions. *Chem. Soc. Rev.* **34**, 1048–1077 (2005). URL http://dx.doi.org/10.1039/B406082M.

[55] Hertel, T., Himmelein, S., Ackermann, T., Stich, D. & Crochet, J. Diffusion limited photoluminescence quantum yields in 1-D semiconductors: Single-wall carbon nanotubes. *ACS Nano* **4**, 7161–7168 (2010). URL http://pubs.acs.org/doi/abs/10.1021/nn101612b. http://pubs.acs.org/doi/pdf/10.1021/nn101612b.

[56] Khripin, C. Y., Manohar, S., Zheng, M. & Jagota, A. Measurement of electrostatic properties of DNA-carbon nanotube hybrids by capillary electrophoresis. *The Journal of Physical Chemistry C* **113**, 13616–13621 (2009). URL http://pubs.acs.org/doi/abs/10.1021/jp903197d. http://pubs.acs.org/doi/pdf/10.1021/jp903197d.

[57] Andrews, D. L. & Demidov, A. A. *Resonance energy transfer / David L. Andrews and Andrey A. Demidov* (New York : Wiley, 1999).

[58] A. G. Mirochnik, V. E. K., N. V. Petrochenkova. Energy transfer in luminescent complexes of EuIII and TbIII with homo- and copolymers of acrylic acid and alkyl methacrylates. *Russian Chemical Bulletin* **45**, 1356 (1995). URL http://link.springer.com/article/10.1007/BF01434212.

[59] Yamase, T. & Naruke, H. Luminescence and energy transfer phenomena in Tb3+/Eu3+ - mixed polyoxometallolanthanoates K15H3 and Na7H19. *The Journal of Physical Chemistry B* **103**, 8850–8857 (1999). URL http://pubs.acs.org/doi/abs/10.1021/jp991536d. http://pubs.acs.org/doi/pdf/10.1021/jp991536d.

[60] Carlson, L. J., Maccagnano, S. E., Zheng, M., Silcox, J. & Krauss, T. D. Fluorescence efficiency of individual carbon nanotubes. *Nano Letters* **7**, 3698–3703 (2007). URL http://pubs.acs.org/doi/abs/10.1021/nl0720142B.

[61] Schoppler, F. *et al.* Molar extinction coefficient of single-wall carbon nanotubes. *The Journal of Physical Chemistry C* **115**, 14682–14686 (2011). URL http://pubs.acs.org/doi/abs/10.1021/jp205289h.

[62] Elbanowski, M., Lis, S. & Konarski, J. Quantum efficiency of the luminescence of Eu(III), Tb(III) and Dy(III) in aqueous solutions. *Monatshefte fur Chemie / Chemical Monthly* **120**, 699–703 (1989). URL http://dx.doi.org/10.1007/BF00809960.

[63] Oosawa, F. *Polyelectrolytes* (Marcel Dekker, New York, 1971).

[64] Manning, G. S. Limiting laws and counterion condensation in polyelectrolyte solutions I. colligative properties. *The Journal of Chemical Physics* **51**, 924–933 (1969). URL http://scitation.aip.org/content/aip/journal/jcp/51/3/10.1063/1.1672157.

[65] Choi, J. H. *et al.* Antidiabetic actions of a non-agonist PPAR[ggr] ligand blocking Cdk5-mediated phosphorylation. *Nature* **477**, 477–481 (2011). URL http://dx.doi.org/10.1038/nature10383.

[66] Gupta, B. K. *et al.* Optical bifunctionality of europium-complexed luminescent graphene nanosheets. *Nano Letters* **11**, 5227–5233 (2011). URL http://pubs.acs.org/doi/abs/10.1021/nl202541n. http://pubs.acs.org/doi/pdf/10.1021/nl202541n.

[67] Posson, D. J., Ge, P., Miller, C., Bezanilla, F. & Selvin, P. R. Small vertical movement of a K+ channel voltage sensor measured with luminescence energy transfer. *Nature* **436**, 848–851 (2005). URL http://dx.doi.org/10.1038/nature03819.

[68] Walter, N. G., Yang, N. & Burke, J. M. Probing non-selective cation binding in the hairpin ribozyme with Tb(III). *Journal of Molecular Biology* **298**, 539 – 555 (2000). URL http://www.sciencedirect.com/science/article/pii/S002228360093691X.

[69] Richardson, F. S. Terbium(III) and europium(III) ions as luminescent probes and stains for biomolecular systems. *Chemical Reviews* **82**, 541–552 (1982). URL http://pubs.acs.org/doi/abs/10.1021/cr00051a004. http://pubs.acs.org/doi/pdf/10.1021/cr00051a004.

[70] Ignatova, T. *et al.* Significant FRET between SWNT/DNA and rare earth ions: A signature of their spatial correlations. *ACS Nano* **5**, 6052–6059 (2011). URL http://pubs.acs.org/doi/abs/10.1021/nn201911b. http://pubs.acs.org/doi/pdf/10.1021/nn201911b.

[71] Wenseleers, W. *et al.* Efficient isolation and solubilization of pristine single-walled nanotubes in bile salt micelles. *Advanced Functional Materials* **14**, 1105–1112 (2004). URL http://dx.doi.org/10.1002/adfm.200400130.

[72] Fagan, J. A. *et al.* Analyzing surfactant structures on length and chirality resolved (6,5) single-wall carbon nanotubes by analytical ultracentrifugation. *ACS Nano* **7**, 3373–3387 (2013). URL http://pubs.acs.org/doi/abs/10.1021/nn4002165.

[73] Liu, Y., Zhang, N., Chen, Y. & Chen, G.-S. Secondary assembly of bile salts mediated by cyclodextrin terbium(III) complex. *Bioorganic & Medicinal Chemistry* **14**, 6615 – 6620 (2006). URL http://www.sciencedirect.com/science/article/pii/S0968089606004512.

[74] Meyerhoffer, S. M. & McGown, L. B. Fluorescent probe studies of metal salt effects on bile salt aggregation. *Journal of the American Chemical Society* **113**, 2146–2149 (1991). URL http://pubs.acs.org/doi/abs/10.1021/ja00006a036. http://pubs.acs.org/doi/pdf/10.1021/ja00006a036.

[75] Neves, A., Valente, A., Burrows, H., Ribeiro, A. & Lobo, V. Effect of terbium(III) chloride on the micellization properties of sodium decyl- and dodecyl-sulfate solutions. *Journal of Colloid and Interface Science* **306**, 166 – 174 (2007). URL http://www.sciencedirect.com/science/article/pii/S0021979706009799.

[76] Duque, J. G. *et al.* New route to fluorescent single-walled carbon nanotube/silica nanocomposites: Balancing fluorescence intensity and environmental sensitivity. *The Journal of Physical Chemistry C* **115**, 15147–15153 (2011). URL http://pubs.acs.org/doi/abs/10.1021/jp2012107.

[77] Moudam, O. *et al.* Europium complexes with high total photoluminescence quantum yields in solution and in PMMA. *Chem. Commun.* 6649–6651 (2009). URL http://dx.doi.org/10.1039/B914978C.

[78] Xiao, M. & Selvin, P. R. Quantum yields of luminescent lanthanide chelates and far-red dyes measured by resonance energy transfer. *Journal of the American Chemical Society* **123**, 7067–7073 (2001). URL http://pubs.acs.org/doi/abs/10.1021/ja0031669.

[79] Chumaevskii, N., Rodnikova, M. & Sirotkin, D. Raman spectra of light and heavy water in the OH and OD stretching vibrations region. *Journal of Molecular Liquids* **82**, 39 – 46 (1999). URL http://www.sciencedirect.com/science/article/pii/S0167732299000409.

[80] Casey, J. P., Bachilo, S. M. & Weisman, R. B. Efficient photosensitized energy transfer and near-ir fluorescence from porphyrin-SWNT complexes. *J. Mater. Chem.* **18**, 1510–1516 (2008). URL http://dx.doi.org/10.1039/B716649D.

[81] Li, S. *et al.* Mobility of polyaromatic hydrocarbons (PAHs) in soil in the presence of carbon nanotubes. *Ecotoxicology and Environmental Safety* **96**, 168 – 174 (2013). URL http://www.sciencedirect.com/science/article/pii/S0147651313003035.

[82] Giese, B., Amaudrut, J., Kohler, A.-K., Spormann, M. & Wessely, S. Direct observation of hole transfer through DNA by hopping between adenine bases and by tunnelling. *Nature* **412**, 318–320 (2001). URL http://dx.doi.org/10.1038/35085542.

[83] Crochet, J. J. *et al.* Free-carrier generation in aggregates of single-wall carbon nanotubes by photoexcitation in the ultraviolet regime. *Phys. Rev. Lett.* **107**, 257402 (2011). URL http://link.aps.org/doi/10.1103/PhysRevLett.107.257402.

[84] Ham, M.-H., Kong, B.-S., Kim, W.-J., Jung, H.-T. & Strano, M. S. Unusually large Franz-Keldysh oscillations at ultraviolet wavelengths in single-walled carbon nanotubes. *Phys. Rev. Lett.* **102**, 047402 (2009). URL http://link.aps.org/doi/10.1103/PhysRevLett.102.047402.

[85] Roxbury, D., Mittal, J. & Jagota, A. Molecular-basis of single-walled carbon nanotube recognition by single-stranded DNA. *Nano Letters* **12**, 1464–1469 (2012). URL http://pubs.acs.org/doi/abs/10.1021/nl204182b.

[86] Wang, F., Wu, Y., Hybertsen, M. S. & Heinz, T. F. Auger recombination of excitons in one-dimensional systems. *Phys. Rev. B* **73**, 245424 (2006). URL http://link.aps.org/doi/10.1103/PhysRevB.73.245424.

[87] Perebeinos, V. & Avouris, P. Phonon and electronic nonradiative decay mechanisms of excitons in carbon nanotubes. *Phys. Rev. Lett.* **101**, 057401 (2008). URL http://link.aps.org/doi/10.1103/PhysRevLett.101.057401.

[88] Zhu, Z. *et al.* Pump-probe spectroscopy of exciton dynamics in (6,5) carbon nanotubes. *The Journal of Physical Chemistry C* **111**, 3831–3835 (2007). URL http://pubs.acs.org/doi/abs/10.1021/jp0669411.

[89] Harrah, D. M. *et al.* Intensity-dependent exciton dynamics of (6,5) single-walled carbon nanotubes: Momentum selection rules, diffusion, and nonlinear interactions. *ACS Nano* **5**, 9898–9906 (2011). URL http://pubs.acs.org/doi/abs/10.1021/nn203604v.

[90] Lefebvre, J., Finnie, P. & Homma, Y. Temperature-dependent photoluminescence from single-walled carbon nanotubes. *Phys. Rev. B* **70**, 045419 (2004). URL http://link.aps.org/doi/10.1103/PhysRevB.70.045419.

[91] Crochet, J. J., Duque, J. G., Werner, J. H. & Doorn, S. K. Photoluminescence imaging of electronic-impurity-induced exciton quenching in single-walled carbon nanotubes. *Nat Nano* **7**, 126–132 (2012). URL http://dx.doi.org/10.1038/nnano.2011.227.

[92] Ghosh, S., Bachilo, S. M., Simonette, R. A., Beckingham, K. M. & Weisman, R. B. Oxygen doping modifies near-infrared band gaps in fluorescent single-walled carbon nanotubes. *Science* **330**, 1656–1659 (2010).

[93] Duque, J. G. *et al.* New route to fluorescent single-walled carbon nanotube/silica nanocomposites: Balancing fluorescence intensity and environmental sensitivity. *The Journal of Physical Chemistry C* **115**, 15147–15153 (2011). URL http://pubs.acs.org/doi/abs/10.1021/jp2012107.

[94] Roxbury, D., Tu, X., Zheng, M. & Jagota, A. Recognition ability of DNA for carbon nanotubes correlates with their binding affinity. *Langmuir* **27**, 8282–8293 (2011). URL http://pubs.acs.org/doi/abs/10.1021/la2007793.

[95] Kinder, J. M. & Mele, E. J. Nonradiative recombination of excitons in carbon nanotubes mediated by free charge carriers. *Phys. Rev. B* **78**, 155429 (2008). URL http://link.aps.org/doi/10.1103/PhysRevB.78.155429.

[96] Matsuda, K., Miyauchi, Y., Sakashita, T. & Kanemitsu, Y. Nonradiative exciton decay dynamics in hole-doped single-walled carbon nanotubes. *Phys. Rev. B* **81**, 033409 (2010). URL http://link.aps.org/doi/10.1103/PhysRevB.81.033409.

[97] D'Souza, F. *et al.* Supramolecular carbon nanotube-fullerene donor-acceptor hybrids for photoinduced electron transfer. *Journal of the American Chemical Society* **129**, 15865–15871 (2007). URL http://pubs.acs.org/doi/abs/10.1021/ja073773x. PMID: 18052162.

[98] Hu, L. *et al.* Light-induced charge transfer in pyrene/CdSe-SWNT hybrids. *Advanced Materials* **20**, 939–946 (2008). URL http://dx.doi.org/10.1002/adma.200701125.

[99] Roca-Sanjuan, D., Rubio, M., Merchan, M. & Serrano-Andras, L. Ab initio determination of the ionization potentials of DNA and RNA nucleobases. *The Journal of Chemical Physics* **125**, – (2006). URL http://scitation.aip.org/content/aip/journal/jcp/125/8/10.1063/1.2336217.

[100] Belau, L., Wilson, K. R., Leone, S. R. & Ahmed, M. Vacuum-ultraviolet photoionization studies of the microhydration of DNA bases (guanine, cytosine,

adenine, and thymine). *The Journal of Physical Chemistry A* **111**, 7562–7568 (2007). URL http://pubs.acs.org/doi/abs/10.1021/jp0705929. PMID: 17419600.

Vita

Personal Information

Education

2007 – 2013: PhD in Physics, Lehigh University, Bethlehem PA, USA
1985 – 1990: B.Sc. and Master Degree (Diploma), major: Radiophysics, Kharkov State University, Kharkov, Ukraine

Career/Employment

2007 – present: Physics Department, Lehigh University
1992 – 2007: B.Verkin Institute for Low Temp. Phys. and Eng. of National Academy of Sciences of Ukraine, Department of Magnetic and Elastic Properties of Solids, Kharkov, Ukraine

Publications during PhD study in peer-reviewed journals

- T. Ignatova, M. Blades, J. A. Fagan, M. Zheng, S.V. Rotkin. Two-color spectroscopy of DNA-SWNT complexes: Photoinduced (π-π^*) DNA autoionization and nonradiative SWNT exciton recombination, currently in production.
- M. Blades, T. Ignatova, J. G. Duque , S. K. Doorn , S. V. Rotkin, Propagation of Terbium Ions Through the SWNT Gel. currently in production.
- T. Ignatova, I. Biaggio, J. G. Duque, S. K. Doorn, S. V. Rotkin. Micelle formation in terbium encapsulated hydrogel: Waterproof photoluminescent

complexes, submitted, under revision.

- T. Ignatova, S. V. Rotkin, Discovering Properties of Nanocarbon Materials as a Pivot for Device Applications, Interface of the Electrochemical Society 22(3), 57-60, 2013.

- T. Ignatova, H. Najafov, A. Ryasnyanskiy, I. Biaggio, M. Zheng, S.V. Rotkin, Significant FRET between SWNT/DNA and rare earth ions: a signature of their spatial correlations. ACS Nano 5(7), 6052-9, 2011.

Book Chapter

T. Ignatova, A.M. Nemilentsau, and S. V. Rotkin, Near-field optics of SWNTs and FRET in their nanoscale complexes, in Handbook on Carbon Nano Materials, ed. F DiSouza, K Kadish. World Scientific Publishing, Inc., Chapter 8, pp. 287-319 (2012). ISBN-10: 981-4401-41-2; ISBN-13: 978-981-4401-41-8.

Conference contributions

- T. Ignatova, J. G. Duque, S. K. Doorn, S. V. Rotkin, Unexpected water screening in gel-encapsulated terbium systems, 2013 APS March Meeting, March 18 - 22, Baltimore, Maryland.

- M. Blades, T. Ignatova, J. G. Duque, S. K. Doorn, S. V. Rotkin, Direct Measurement of Diffusion of Terbium Ions Through a Silica Gel Matrix, 2013 APS March Meeting, March 18 - 22, Baltimore, Maryland.

- T. Ignatova, and S. V. Rotkin, A Signature of Spatial Correlations between rare earth ions and single-wall nanotubes wrapped with DNA in their mixed solution, 2012 APS March Meeting, Feb 27 - March 2, Boston, Massachusetts.

- T. Flores, M. Pirbhai, T. Ignatova, S. V. Rotkin, Identification of Single Wall Carbon Nanotubes Using Advanced Microscopy Techniques: AFM, PLE,

TIRFM, The Joint Annual Conferences of the National Society of Black Physicists and the National Society of Hispanic Physicists, Sep 21-24, 2011, Austin, TX.

- M. Blades, M. Pirbhai, T. Ignatova, and S. V. Rotkin, Construction of an Epifluorescent Microscope for Use in Imaging Carbon Nanotubes, 10th Annual Open House of the Center for Optical Technologies, November 21, 2011, Lehigh University.

- T. Flores, M. Pirbhai, T. Ignatova, S. V. Rotkin, Identification of Single Wall Carbon Nanotubes Using Advanced Microscopy Techniques: AFM, PLE, TIRFM, The Joint Annual Conferences of the National Society of Black Physicists and the National Society of Hispanic Physicists, Sep 21-24, 2011, Austin, TX.

- T. Ignatova, D. Pristinski, S. V Rotkin, Photoexcitation of SWNT through the DNA-Rare Earth Brige, Gotham Metro Condensed Matter Meeting, April 15, 2011 The New York Academy of Sciences.

- T. Ignatova, D. Pristinski and S. V. Rotkin, Studying of kinetics of rear earth ion (REI) nanoscale complex formation by resonant energy transfer, 2011 APS March Meeting, March 2125, 2011; Dallas, Texas. [Bulletin of the APS March Meeting, 56 (1), A28.00012 (2011).]

- T. Ignatova, H. Najafov and S. V. Rotkin, Experimental study of the resonance energy transfer rate between Rare Earth ions and Carbon Nanotubes, the 217th ECS Meeting, April 25-30, 2010, Vancouver, Canada.

- T. Ignatova, H. Najafov and S.a V. Rotkin, Confirmation of the resonance energy transfer between Rare Earth-DNA-Carbon Nanotube complex, 2010 APS March Meeting, March 1519, 2010; Portland, Oregon. [Bulletin of the APS March Meeting, 55 (2), A20.00007 (2010).]

- T. Ignatova, H. Najafov, A.Ryasnyanskiy, I. Biaggio and S. V. Rotkin, Chirality dependence of Resonance Energy Transfer between Single Wall Nanotubes

(SWNT) and Rear Earth Ions (REI), 9th Annual Open House of the Center for Optical Technologies, October 11-12, 2010, Lehigh University.

- T. Ignatova, H. Najafov and S. V. Rotkin, Experimental Study of the Resonance Energy Transfer Rate Between Rare Earth Ions and Carbon Nanotubes, Nano-Energy Workshop, Lehigh University; Sep 13-14, 2010.

- T. Ignatova, H. Najafov and S. V. Rotkin, Energy transfer between Rear Earth ions and Carbon Nanotubes, 2009 APS March Meeting, March 1620, 2009; Pittsburgh, PA.

- T. Ignatova, H.Najafov and S. V. Rotkin, Energy transfer of resonance type between rear earth ions (RE) and Carbon Nanotubes (CNT), 7th Annual Open House of the Center for Optical Technologies, October 13-14, 2008, Lehigh University.